Computational Geosciences (2020) 24:1141–1161
https://doi.org/10.1007/s10596-019-09930-8

ORIGINAL PAPER

Velocity postprocessing schemes for multiscale mixed methods applied to contaminant transport in subsurface flows

Rafael T. Guiraldello[1] · Roberto F. Ausas[1] · Fabricio S. Sousa[1] · Felipe Pereira[2] · Gustavo C. Buscaglia[1]

Received: 27 March 2019 / Accepted: 16 December 2019 / Published online: 20 February 2020

Abstract

We propose two postprocessing procedures (*Patch* method and *Stitch* method) to recover local conservation of velocity fields produced by multiscale approximations that are only conservative in coarse scales. These procedures operate on small overlapping regions and are designed to be implemented in parallel, which makes them relatively inexpensive. We investigate the applicability of such methods when tested on single-phase flow problems using the Multiscale Robin Coupled Method (MRCM) in highly heterogeneous permeability fields for modeling the contaminant transport in the subsurface. Numerical simulations are presented aiming to illustrate and compare the performance of the new methods with a standard procedure, the *Mean* method, in terms of accuracy in contaminant concentration. We show that for a collection of permeability fields taken as log-normal fields, the new postprocessing procedures provide similar or better accuracy than the Mean method. Then, we turn our attention to flows in high-contrast channelized porous formations, where the new methods robustly yield more accurate results and should thus be favored.

Keywords Porous media · Darcy flow · Contaminant transport · Multiscale approximation · Domain decomposition · Compatibility conditions · Downscaling · Velocity postprocessing

1 Motivation

We are concerned with flows in porous media. The model problem that we consider consists on the one hand of the second order elliptic Darcy model, whose mixed form is: find $\mathbf{u}$ and p such that

$$\begin{cases} \mathbf{u} = -K\,\nabla p & \text{in } \Omega \\ \nabla\cdot\mathbf{u} = f & \text{in } \Omega \\ p = g & \text{on } \partial\Omega_p \\ \mathbf{u}\cdot\check{\mathbf{n}}_{\partial\Omega} = z & \text{on } \partial\Omega_u \end{cases} \tag{1}$$

where $\Omega \subset \mathbb{R}^d$, $d = 2$ or 3 is the computational domain, K is a symmetric, uniformly positive definite tensor with components in $L^\infty(\Omega)$, $\mathbf{u}$ is the Darcy velocity, p is the pressure, $f \in L^2(\Omega)$ the source, $g \in H^{\frac{1}{2}}(\partial\Omega_p)$ the pressure boundary data, $z \in H^{-\frac{1}{2}}(\partial\Omega_u)$ the normal velocity data and $\check{\mathbf{n}}_{\partial\Omega}$ is the outer normal to $\partial\Omega$. On the other hand, given the fluid velocity $\mathbf{u}$ as obtained from (1), we solve the transport of a passive tracer or contaminant which is governed by the scalar hyperbolic conservation law

$$\begin{cases} \dfrac{\partial \mathcal{C}}{\partial t} + \nabla\cdot(\mathbf{u}\,\mathcal{C}) = 0 & \text{in } \Omega \\ \mathcal{C}(\mathbf{x}, t=0) = \mathcal{C}_0(\mathbf{x}) & \text{in } \Omega \\ \mathcal{C}(\mathbf{x}, t) = \mathcal{C}_D(\mathbf{x}, t) & \text{in } \partial\Omega^- \end{cases} \tag{2}$$

where $\mathcal{C}$ is the concentration of the pollutant species, $\mathcal{C}_0$ its initial condition and $\mathcal{C}_D$ the concentration at the inlet boundaries $\partial\Omega^- = \{\mathbf{x} \in \partial\Omega,\ \mathbf{u}\cdot\check{\mathbf{n}}_{\partial\Omega} < 0\}$.

✉ Roberto F. Ausas
rfausas@icmc.usp.br

Rafael T. Guiraldello
rafaeltrevisanuto@gmail.com

Fabricio S. Sousa
fsimeoni@icmc.usp.br

Felipe Pereira
luisfelipe.pereira@utdallas.edu

Gustavo C. Buscaglia
gustavo.buscaglia@icmc.usp.br

[1] Instituto de Ciências Matemáticas e de Computação, Universidade de São Paulo, Av. Trabalhador São-carlense, 400, São Carlos, SP, 13566-590, Brazil

[2] Department of Mathematical Sciences, The University of Texas at Dallas, 800 W. Campbell Road, Richardson, TX, 75080-3021, USA

Nowadays applications of fluid flow in subsurface problems governed by (1)–(2) or some variant of it, such as those involving oil and gas production, compositional flow in oil reservoirs and pollutant transport in aquifers, may require over a billion computational cells to predict with reasonable accuracy the flow variables. Besides this enormous challenge, uncertainty quantification studies are necessary to deal with the stochastic nature of the permeability field and estimate relevant quantities with statistical significance. Multiscale domain decomposition methods for the simulation of transport in porous media, aiming for high performance and scalability, have been the focus of intensive research over the last years. The underlying idea is to decompose the computational domain into non-overlapping subdomains in which local small problems are solved. This is naturally done in parallel. Recently, in [1] and [2], we have proposed a new method named Multiscale Robin Coupled Method (MRCM) as a generalization to the Multiscale Mixed Method (MuMM) [3], based on a domain decomposition technique introduced originally by Douglas et al. [4], in which the local problems are subject to Robin type boundary conditions. In the new method we introduce two unknown fields on the so-called skeleton of the domain decomposition, namely, a flux U_H and a pressure P_H, belonging to some function spaces of low dimension $\mathcal{U}_H$ and $\mathcal{P}_H$ defined over the skeleton, such that continuity of pressure and flux are weakly enforced. This in turn leads to a system of equations of intermediate size that couples the solutions over the domains of the decomposition. In a multiscale formulation like ours, the compatibility conditions are only satisfied at some coarse scale $H \gg h$ in order to alleviate the computational burden. Denoting the skeleton of the decomposition by Γ and by $(\mathbf{u}, p)$ the multiscale solution, this means that

$$\int_\Gamma \left(\mathbf{u}^+ - \mathbf{u}^-\right) \cdot \check{\mathbf{n}}\, M_H \, d\Gamma \;=\; 0\,, \qquad \forall\, M_H \,\in\, \mathcal{P}_H\,, \quad (3)$$

$$\int_\Gamma (p^+ - p^-)\, V_H \, d\Gamma \;=\; 0\,, \qquad \forall\, V_H \,\in\, \mathcal{U}_H\,, \quad (4)$$

where the $+$ and $-$ superscripts refer to the two-sided limits approaching Γ and $\check{\mathbf{n}}$ is a unit vector normal to Γ. In the limit case when $H = h$ we recover the global fine grid solution and continuity of flux and pressure is satisfied pointwise. Two well-known methods, the Multiscale Mortar Mixed Finite Element Method (MMMFEM) [5] and the Multiscale Hybrid-Mixed Finite Element Method (MHM) [6] can be obtained as particular cases of the MRCM by suitably defining a parameter α in the Robin boundary condition that couples the subdomain solutions, i.e.,

$$-\frac{\alpha\, H}{K_i(\mathbf{x})}\, \mathbf{u}_h^i \cdot \check{\mathbf{n}}^i + p^i = -\frac{\alpha\, H}{K_i(\mathbf{x})}\, U_H\, \check{\mathbf{n}} \cdot \check{\mathbf{n}}^i + P_H \quad (5)$$

where $\mathbf{u}_h^i$ is the flux multiscale solution on subdomain Ω_i and $\check{\mathbf{n}}^i$ is the exterior normal to $\partial\Omega_i$. We can switch from one method to the other in different parts of the domain without any implementation effort. Also, there is considerable freedom to select the numerical schemes to solve the local problems in the subdomains as well as to choose the interface spaces $\mathcal{U}_H$ and $\mathcal{P}_H$ independently from each other. All these features give the possibility of producing more accurate solutions as compared to other available techniques, as we have numerically shown in [1, 2]. The drawback of course is that fluxes are only conservative at the coarse scale given by the size of the subdomains H, i.e., for each interface Γ_{ij} between subdomains Ω_i and Ω_j the following holds

$$\int_{\Gamma_{ij}} \mathbf{u}_h^i \cdot \check{\mathbf{n}}\, d\Gamma = \int_{\Gamma_{ij}} \mathbf{u}_h^j \cdot \check{\mathbf{n}}\, d\Gamma. \quad (6)$$

Fluxes are not in general continuous at the fine level of the discretization on interfaces between adjacent domains. The velocity field produced by such methods is unsuitable to be used in the transport equation (2). Therefore, some postprocessing or downscaling procedure becomes necessary.

Let us illustrate this with an example. Consider the highly heterogeneous permeability field displayed in Fig. 1. This field exhibits a contrast $K_{\max}/K_{\min} \sim 10^5$ and corresponds to a log-normal field plus a central channelized region that has been inserted by hand to make the problem more challenging. In this example, the domain $\Omega = [0, 1] \times [0, 1]$ is discretized into 100×100 fine grid cells and decomposed into 2×2 subdomains. The skeleton of the decomposition is denoted by Γ, which in this particular case is made of the four internal interfaces between the subdomains.

Figure 2 shows the multiscale solution (velocity and pressure) produced by our method in three different situations, considering interface spaces $\mathcal{P}_H$ and $\mathcal{U}_H$ of very low dimension made up of functions that are constant by parts on each interface. In the first case (top subfigure), we take the Robin condition parameter very large ($\alpha = 10^6$). In this situation the MRCM retrieves the MHM solution, in which continuity of fluxes is enforced pointwise, as observed in the insert, whereas continuity of pressure is weakly satisfied according to (4). This leads to a significant pressure jump at the interfaces, also clearly noticeable in the figure. In the second case we take $\alpha = 1$ (middle part). For such intermediate value of the Robin condition parameter neither flux nor pressure satisfy pointwise continuity. As a result, a small jump is observed at the interfaces in both multiscale velocity and pressure. For instance, this is clearly noticed in the right insert, where we have also plotted the flux jump along Γ_{13} which is one of the critical interfaces crossing the high permeability channel. Finally, we take the algorithmic parameter very small ($\alpha = 10^{-6}$),

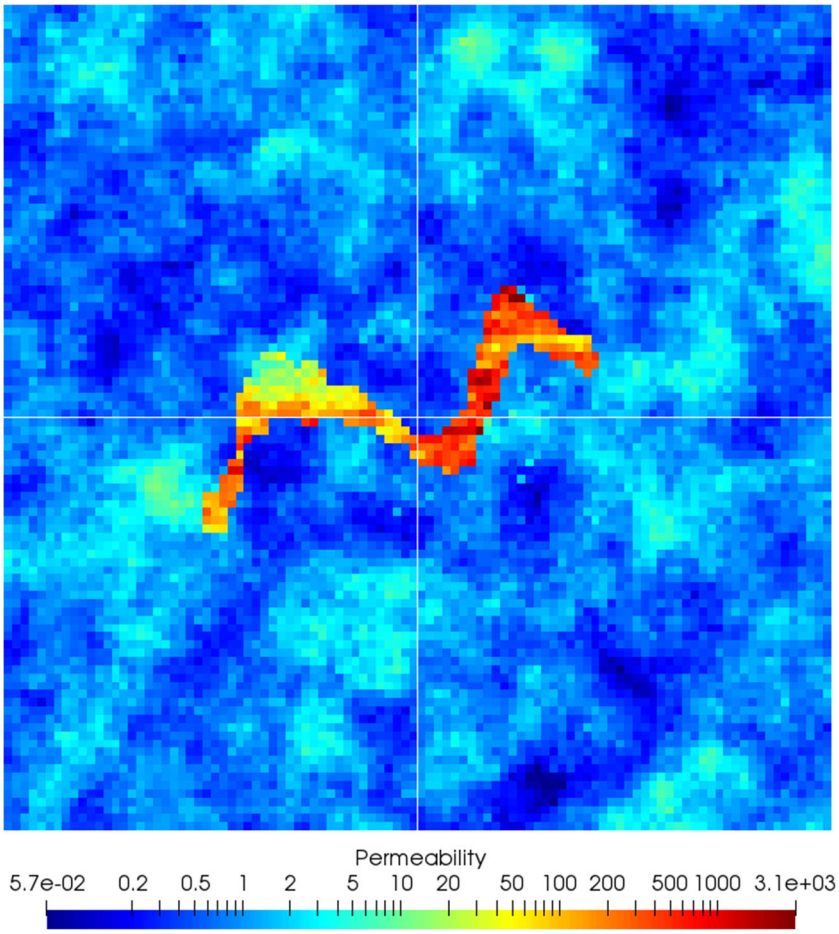

Fig. 1 Permeability field used to illustrate the behavior of the multiscale method

such that the method retrieves the MMMFEM solution, in which the pressure field is continuous, as observed at the bottom of Fig. 2, while the velocity field exhibits very large jumps at the interfaces, also highlighted in the right insert that shows the flux jump along interface Γ_{13}. It becomes evident that in the last two cases some downscaling or postprocessing procedure on the velocity field is mandatory prior to its use in the resolution of the transport equation, be it in a multiphase (non-linear) problem or in the linear case of a passive tracer. This is addressed in this article where two new simple and relatively inexpensive procedures are proposed, namely the *Patch* method and the *Stitch* method, that are compared to the standard technique of computing the average velocity at interfaces between subdomains. Although, we restrict in this article the application of the new postprocessing methods to multiscale solutions produced by the MRCM (and as particular cases, the MMMFEM and MHM), they can be readily applied to any multiscale method, provided its solution is conservative at the coarse scale of the domain decomposition. The proposed methods share ideas with the postprocessing techniques introduced in [7, 8] and the procedures applied in [9, 10], except that we do not rely on artificial source terms to balance the net flow of the new computed fluxes on subdomain interfaces. Also, our methods share similarities with the procedure proposed in [3], however, in their case the postprocessing scheme is not suitably designed to be implemented in parallel.

After this introduction, the plan of the article is as follows. First, we recall the MRCM method by explaining with some level of detail how the previous example was actually computed. In Section 3 the proposed downscaling methods are presented. In the numerical results sections 4-5 we extensively assess and compare them by solving the transport of a passive tracer by means of a finite volume method in highly heterogeneous permeability rock formations. Finally, some conclusions are drawn.

2 The multiscale Robin coupled method

In this section we recall the main ingredients and some implementation aspects of the multiscale Robin coupled method. For further details, such as well-posedness results,

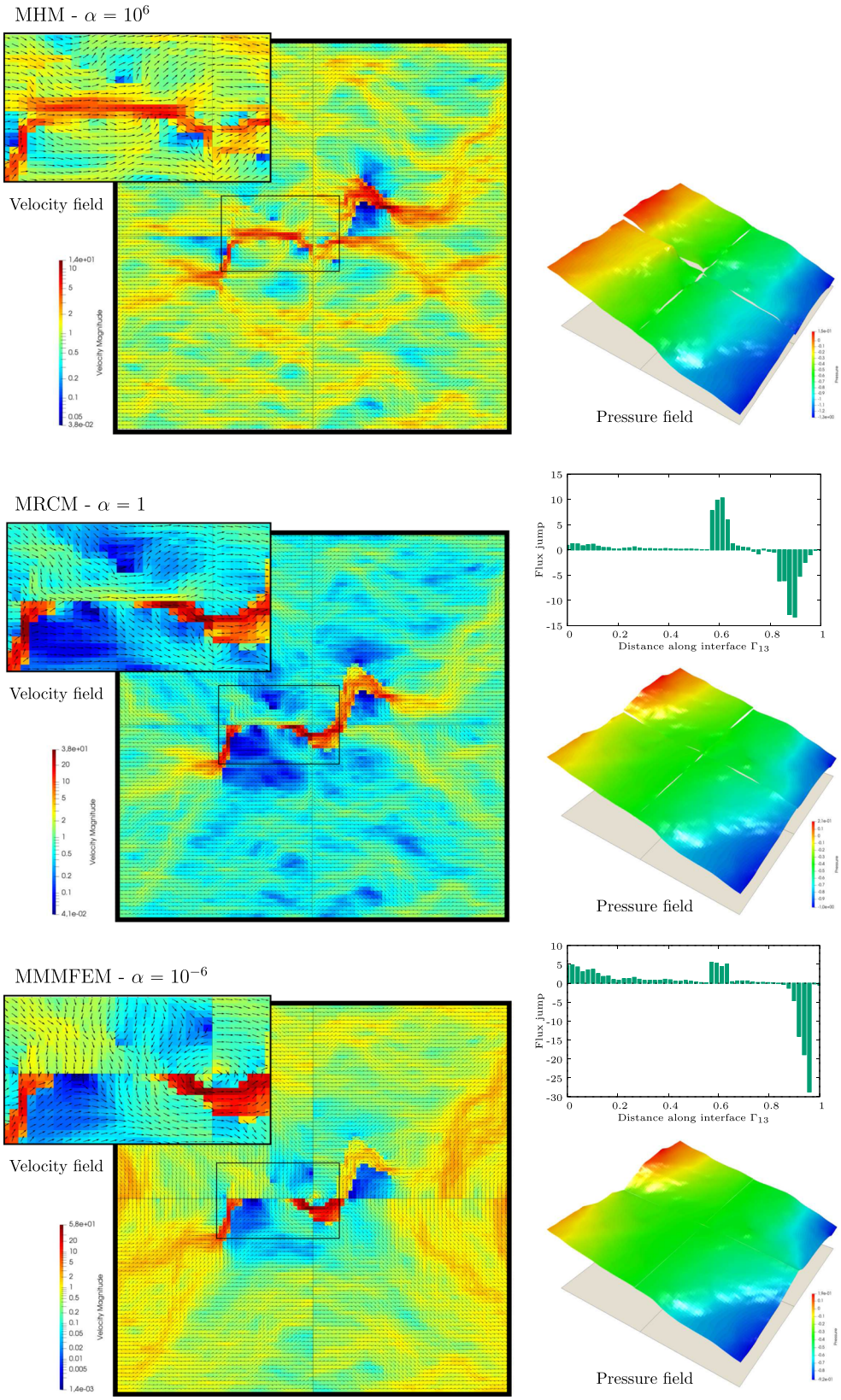

Fig. 2 Multiscale solutions produced by the MRCM method considering different values of the Robin condition parameter: $\alpha = 10^6$ (top), $\alpha = 1$ (middle), $\alpha = 10^{-6}$ (bottom)

implementation in a variational setting, and the possibility of using informed functions to build up the interface spaces $\mathcal{U}_H$ and $\mathcal{P}_H$, the reader is referred to [1, 2].

We begin by introducing some notation. The key ingredient is the discrete solution of local Darcy problems. Let us consider a rectangular domain $\Omega \subset \mathbb{R}^d$, $d = 2, 3$ and a subdivision $\mathcal{T}_h$ made of d-dimensional rectangles. We refer to this partition as the *fine grid*. The permeability K and source term f are functions belonging to the space $P_0(\mathcal{T}_h)$, i.e., functions that are constant by parts on this fine grid. In general, the boundary of Ω can be divided into disjoint parts denoted by $\Gamma_u, \Gamma_p, \Gamma_r$ in which flux, pressure and Robin boundary conditions are imposed. The problem reads: Find $(\mathbf{u}_h, p_h)$ such that

$$\begin{cases} \mathbf{u}_h = -K\nabla p_h & \text{in } \Omega \\ \nabla\cdot\mathbf{u}_h = f & \text{in } \Omega \\ p_h = g_p & \text{on } \Gamma_p \\ \mathbf{u}_h\cdot\mathbf{n} = g_u & \text{on } \Gamma_u \\ -\beta\mathbf{u}_h\cdot\mathbf{n} + p = g_r & \text{on } \Gamma_r \end{cases} . \tag{7}$$

The domain Ω can be the domain in which the global problem being considered is posed or any subdomain made of a collection of fine grid cells, as it will be the case later on when describing the downscaling procedures. Figure 3 shows the computational domain, the fine grid discretization and the domain decomposition. For the solution of the Darcy problems, we adopt a standard cell-centered finite volume scheme on rectangular cartesian grids in which we solve for the cell pressure unknowns $p_{I,J}$ by eliminating the edge flux unknowns $u_{I\pm\frac{1}{2},J\pm\frac{1}{2}}$. A complete description can be found in [1] (for further details and possible generalizations, see, e.g., [11]). As mentioned, there is considerable freedom to choose the local solvers. In principle any finite volume, finite element or finite difference scheme that delivers the edge fluxes at subdomain interfaces, when requested by the multiscale method to be described below, can be used.

A non-overlapping domain decomposition of Ω into subdomains Ω_i, $i = 1, \ldots, N$ is considered. Let us denote by $\check{\mathbf{n}}^i$ the outer normal to $\partial\Omega^i$ and by $\check{\mathbf{n}}$ a unique normal

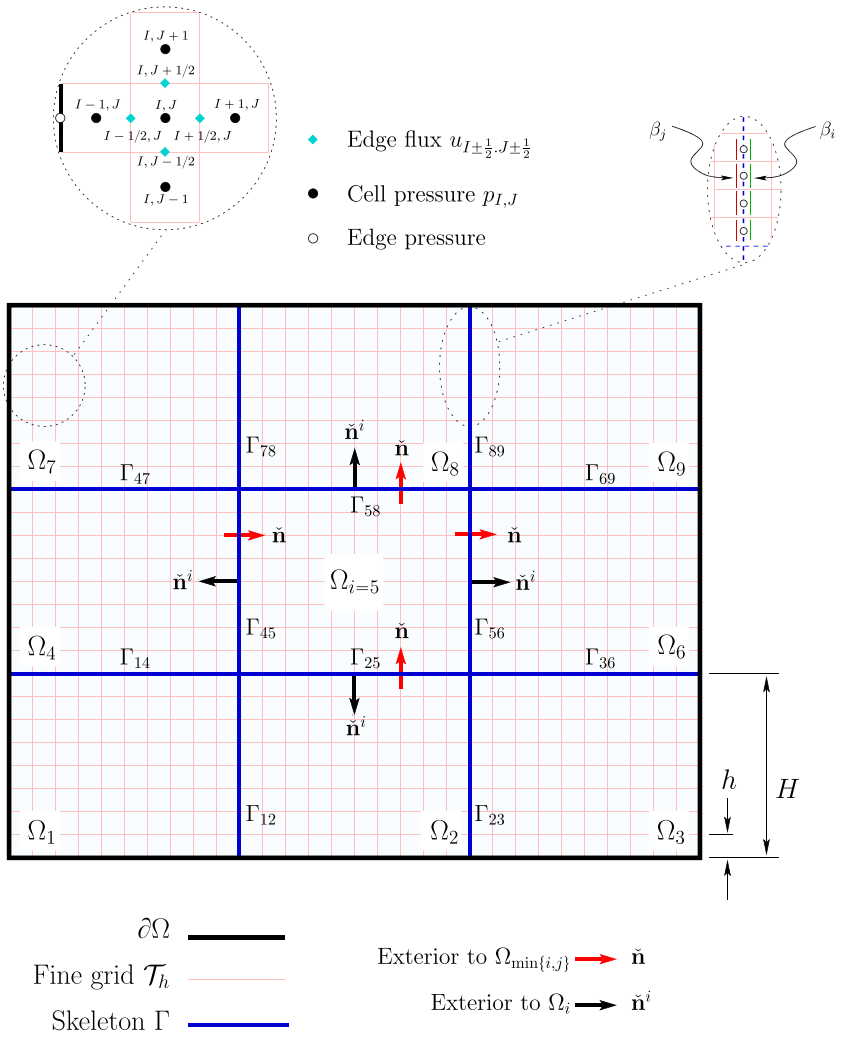

Fig. 3 The computational domain along with the fine grid discretization and the domain decomposition adopted

to the interface Γ_{ij} defined such that it points out from the domain with smallest index (i.e., $\check{\mathbf{n}} = \check{\mathbf{n}}^{\min(i,j)}$).

Our multiscale method can be written as: Find subdomain solutions $(\mathbf{u}_h^i, p_h^i)$, $i = 1, \ldots, N$ and interface fields (U_H, P_H) satisfying the local problems

$$\left\{\begin{array}{rcll} \mathbf{u}_h^i &=& -K\,\nabla p_h^i & \text{in } \Omega_i \\ \nabla\cdot\mathbf{u}_h^i &=& f & \text{in } \Omega_i \\ p_h^i &=& g_p & \text{on } \partial\Omega_i\cap\Gamma_p \\ \mathbf{u}_h^i\cdot\check{\mathbf{n}}^i &=& g_u & \text{on } \partial\Omega_i\cap\Gamma_u \\ -\beta_i\mathbf{u}_h^i\cdot\check{\mathbf{n}}^i + p_h^i &=& -\beta_i U_H\,\check{\mathbf{n}}\cdot\check{\mathbf{n}}^i + P_H & \text{on } \partial\Omega_i\cap\Gamma \end{array}\right. \tag{8}$$

in which the differential operators are replaced by suitable discrete approximations, together with the compatibility conditions on the skeleton Γ

$$\left\{\begin{array}{l} \displaystyle\sum_{i=1}^{N}\int_{\partial\Omega_i\cap\Gamma}\left(\mathbf{u}_h^i\cdot\check{\mathbf{n}}^i\right)\psi\,d\Gamma = 0\,, \\ \displaystyle\sum_{i=1}^{N}\int_{\partial\Omega_i\cap\Gamma}\beta_i\left(\mathbf{u}_h^i\cdot\check{\mathbf{n}}^i - U_H\,\check{\mathbf{n}}^i\cdot\check{\mathbf{n}}\right)\phi\,\check{\mathbf{n}}^i\cdot\check{\mathbf{n}}\,d\Gamma = 0\,, \end{array}\right. \tag{9}$$

which must hold for all functions $\psi \in \mathcal{P}_H$ and $\phi \in \mathcal{U}_H$. The interface flux U_H and interface pressure P_H are functions belonging to spaces $\mathcal{P}_H$ and $\mathcal{U}_H$, respectively, which are contained in $F_h(\mathcal{E}_h)$ defined as

$$F_h(\mathcal{E}_h) = \{f : \mathcal{E}_h \to \mathbb{R} \mid f|_e \in \mathbb{P}_0\,,\ \forall\, e \in \mathcal{E}_h\}\,, \tag{10}$$

where $\mathcal{E}_h$ is the set of all edges (in 2D) or faces (in 3D) of $\mathcal{T}_h$ contained in Γ. These spaces are made up at least of the constant function over Γ. Equation (9) in such case is nothing but the statement that fluxes and pressures are continuous over Γ in the mean sense. A smart definition of the interface spaces is essential for the resulting accuracy and convergence of the method. In this article we restrict ourselves to polynomial spaces for simplicity, however some better strategies were recently devised in [2]. As for the Robin condition parameter β_i on each subdomain, several choices are possible. Based on our previous experience (see [2]), we adopt

$$\beta_i(\mathbf{x}) = \frac{\alpha\, H}{K_i(\mathbf{x})} \tag{11}$$

where α is a dimensionless algorithmic parameter that is taken equal to 1 in the numerical experiments below, H is the characteristic size of the subdomains and $K_i(\mathbf{x})$ is a local permeability. By changing α, we retrieve the MMMFEM method ($\alpha \to 0$) and the MHM method ($\alpha \to \infty$) [1].

Let us explain how the example of the previous section was actually computed by using the MRCM formulation. First, to solve the problem efficiently we must segregate the resolution of the subdomain problems from the resolution of the interface unknowns. To that end, on each subdomain Ω_i, the solution $(\mathbf{u}_h^i, p_h^i)$ of the Darcy problem is decomposed as the sum of two parts

$$\mathbf{u}_h^i = \widehat{\mathbf{u}}_h^i + \overline{\mathbf{u}}_h^i, \qquad p_h^i = \widehat{p}_h^i + \overline{p}_h^i, \tag{12}$$

satisfying the following problems

$$\left\{\begin{array}{rcll} \overline{\mathbf{u}}_h^i &=& -K\,\nabla\overline{p}_h^i & \text{in } \Omega_i \\ \nabla\cdot\overline{\mathbf{u}}_h^i &=& f & \text{in } \Omega_i \\ \overline{p}_h^i &=& g_p & \text{on } \partial\Omega_i\cap\Gamma_p \\ \overline{\mathbf{u}}_h^i\cdot\check{\mathbf{n}}^i &=& g_u & \text{on } \partial\Omega_i\cap\Gamma_u \\ -\beta_i\overline{\mathbf{u}}_h^i\cdot\check{\mathbf{n}}^i + \overline{p}_h^i &=& 0 & \text{on } \partial\Omega_i\cap\Gamma \end{array}\right. , \tag{13}$$

$$\left\{\begin{array}{rcll} \widehat{\mathbf{u}}_h^i &=& -K\,\nabla\widehat{p}_h^i & \text{in } \Omega_i \\ \nabla\cdot\widehat{\mathbf{u}}_h^i &=& 0 & \text{in } \Omega_i \\ \widehat{p}_h^i &=& 0 & \text{on } \partial\Omega_i\cap\Gamma_p \\ \widehat{\mathbf{u}}_h^i\cdot\check{\mathbf{n}}^i &=& 0 & \text{on } \partial\Omega_i\cap\Gamma_u \\ -\beta_i\widehat{\mathbf{u}}_h^i\cdot\check{\mathbf{n}}^i + \widehat{p}_h^i &=& -\beta_i U_H\,\check{\mathbf{n}}\cdot\check{\mathbf{n}}^i + P_H & \text{on } \partial\Omega_i\cap\Gamma \end{array}\right. . \tag{14}$$

It is useful to think about the solution $\widehat{\mathbf{u}}_h^i$ as a function of the interface data (P_H, U_H). Abusing notation this will be denoted later on as $\widehat{\mathbf{u}}_h^i(P_H, U_H)$. In the example above, the skeleton Γ in which the Robin boundary conditions are being imposed is made of the four internal interfaces as shown in Fig. 1, which are numbered Γ_{12}, Γ_{34}, Γ_{13} and Γ_{24}.

Now, consider $\mathcal{P}_H = \text{span}\{\psi_1, \ldots, \psi_{N_P}\}$ and $\mathcal{U}_H = \text{span}\{\phi_1, \ldots, \phi_{N_U}\}$, where N_P and N_U are the dimensions of the interface spaces. In general, we choose k_U and k_P degrees of freedom per interface, therefore the dimensions of these spaces are $N_P = k_P \times N_I$ and $N_U = k_U \times N_I$, being N_I the number of elements in the skeleton mesh. The simplest case corresponds to taking $k_P = k_U = 1$ and one element per interface between subdomains, as we have done in the example above. In such case, the interface spaces are made up of functions that are constant on each interface Γ_{ij}. Let us write the interface fields as linear combinations of the basis functions

$$P_H = \sum_{k=1}^{N_P} P_k\,\psi_k, \quad U_H = \sum_{k=1}^{N_U} U_k\,\phi_k. \tag{15}$$

This leads to the linear system of equations to be satisfied by the vector of interface unknown coefficients $\underline{X} = (P_1, \ldots, P_{N_P}, U_1, \ldots, U_{N_U})^\intercal$. This system consists of two blocks of rows and columns

$$\underline{\underline{A}}\,\underline{X} = \underline{b} \to \begin{bmatrix} A^{PP} & A^{PU} \\ A^{UP} & A^{UU} \end{bmatrix}\begin{bmatrix} \underline{P} \\ \underline{U} \end{bmatrix} = \begin{bmatrix} \underline{b}^P \\ \underline{b}^U \end{bmatrix}. \tag{16}$$

The first block of rows is obtained by taking $\psi = \psi_\ell,\ \ell = 1, \ldots, N_P$ in the first equation of (9), i.e.,

$$\begin{aligned}
0 &= \sum_{i=1}^{N} \int_{\partial\Omega_i \cap \Gamma} \left(\mathbf{u}_h^i \cdot \check{\mathbf{n}}^i\right) \psi_\ell = \sum_{\substack{ij \\ i<j}} \int_{\Gamma_{ij}} \left(\mathbf{u}_h^i \cdot \check{\mathbf{n}}^i + \mathbf{u}_h^j \cdot \check{\mathbf{n}}^j\right) \psi_\ell \\
&= \sum_{\substack{ij \\ i<j}} \int_{\Gamma_{ij}} \left[\left(\widehat{\mathbf{u}}_h^i(P_H, U_H) + \overline{\mathbf{u}}_h^i\right) \cdot \check{\mathbf{n}}^i + \left(\widehat{\mathbf{u}}_h^j(P_H, U_H) + \overline{\mathbf{u}}_h^j\right) \cdot \check{\mathbf{n}}^j\right] \psi_\ell \\
&= \sum_{\substack{ij \\ i<j}} \int_{\Gamma_{ij}} \left(\widehat{\mathbf{u}}_h^i(P_H, U_H) - \widehat{\mathbf{u}}_h^j(P_H, U_H)\right) \cdot \check{\mathbf{n}}\, \psi_\ell \\
&\quad + \sum_{\substack{ij \\ i<j}} \int_{\Gamma_{ij}} \left(\overline{\mathbf{u}}_h^i - \overline{\mathbf{u}}_h^j\right) \cdot \check{\mathbf{n}}\, \psi_\ell, \qquad (17)
\end{aligned}$$

where we have emphasized the dependence of $\widehat{\mathbf{u}}_h^i$ with respect to (P_H, U_H) and omitted the differential $d\Gamma$ for conciseness. Using (15), we obtain

$$\begin{aligned}
&\underbrace{\sum_{k=1}^{N_P} P_k \sum_{\substack{ij \\ i<j}} \int_{\Gamma_{ij}} \mathcal{J}_{ij}\left(\widehat{\mathbf{u}}_h(\psi_k, 0)\right) \psi_\ell}_{A_{\ell k}^{PP}} \\
&+ \underbrace{\sum_{k=1}^{N_U} U_k \sum_{\substack{ij \\ i<j}} \int_{\Gamma_{ij}} \mathcal{J}_{ij}\left(\widehat{\mathbf{u}}_h(0, \phi_k)\right) \psi_\ell}_{A_{\ell k}^{PU}} \\
&= \underbrace{-\sum_{\substack{ij \\ i<j}} \int_{\Gamma_{ij}} \mathcal{J}_{ij}(\overline{\mathbf{u}}_h)\, \psi_\ell}_{b_\ell^P}, \qquad (18)
\end{aligned}$$

where the symbol $\mathcal{J}_{ij}(\cdot)$ stands for the jump operator at Γ_{ij} and is defined for any vector field $\mathbf{v}$ as $\mathcal{J}_{ij}(\mathbf{v}) = (\mathbf{v}^i - \mathbf{v}^j) \cdot \check{\mathbf{n}}$. The second block of rows is obtained similarly by taking $\phi = \phi_\ell,\ \ell = 1, \ldots, N_U$ in the second equation of (9), i.e.,

$$\begin{aligned}
0 &= \sum_{i=1}^{N} \int_{\partial\Omega_i \cap \Gamma} \beta_i \left(\mathbf{u}_h^i \cdot \check{\mathbf{n}}^i - U_H\, \check{\mathbf{n}}^i \cdot \check{\mathbf{n}}\right) \phi_\ell\, \check{\mathbf{n}}^i \cdot \check{\mathbf{n}} \\
&= \sum_{\substack{ij \\ i<j}} \int_{\Gamma_{ij}} \left(\beta_i\, \mathbf{u}_h^i + \beta_j\, \mathbf{u}_h^j\right) \cdot \check{\mathbf{n}}\, \phi_\ell - \sum_{\substack{ij \\ i<j}} \int_{\Gamma_{ij}} \left(\beta_i + \beta_j\right)\, U_H\, \phi_\ell \\
&= \sum_{\substack{ij \\ i<j}} \int_{\Gamma_{ij}} \left(\beta_i\, \widehat{\mathbf{u}}_h^i(P_H, U_H) + \beta_j\, \widehat{\mathbf{u}}_h^j(P_H, U_H)\right) \cdot \check{\mathbf{n}}\, \phi_\ell \\
&\quad + \sum_{\substack{ij \\ i<j}} \int_{\Gamma_{ij}} \left(\beta_i\, \overline{\mathbf{u}}_h^i + \beta_j\, \overline{\mathbf{u}}_h^j\right) \cdot \check{\mathbf{n}}\, \phi_\ell - \sum_{\substack{ij \\ i<j}} \int_{\Gamma_{ij}} \left(\beta_i + \beta_j\right)\, U_H\, \phi_\ell. \qquad (19)
\end{aligned}$$

Again, inserting (15) yields

$$\begin{aligned}
&\underbrace{\sum_{k=1}^{N_P} P_k \sum_{\substack{ij \\ i<j}} \int_{\Gamma_{ij}} \left(\beta_i\, \widehat{\mathbf{u}}_h^i(\psi_k, 0) + \beta_j\, \widehat{\mathbf{u}}_h^j(\psi_k, 0)\right) \cdot \check{\mathbf{n}}\, \phi_\ell}_{A_{\ell k}^{UP}} \\
&+ \underbrace{\sum_{k=1}^{N_U} U_k \sum_{\substack{ij \\ i<j}} \int_{\Gamma_{ij}} \left[\left(\beta_i\, \widehat{\mathbf{u}}_h^i(0, \phi_k) + \beta_j\, \widehat{\mathbf{u}}_h^j(0, \phi_k)\right) \cdot \check{\mathbf{n}} - \left(\beta_i + \beta_j\right)\, \phi_k\right] \phi_\ell}_{A_{\ell k}^{UU}} \\
&= \underbrace{-\sum_{\substack{ij \\ i<j}} \int_{\Gamma_{ij}} \left(\beta_i\, \overline{\mathbf{u}}_h^i + \beta_j\, \overline{\mathbf{u}}_h^j\right) \cdot \check{\mathbf{n}}\, \phi_\ell}_{b_\ell^U}. \qquad (20)
\end{aligned}$$

Remark 1 Two remarks can be made about (18) and (20):

i. The functions $\widehat{\mathbf{u}}_h^i(\psi_k, 0)$ and $\widehat{\mathbf{u}}_h^i(0, \phi_k)$ are the solutions to the subdomain problems (14) taking as Robin boundary data $(P_H, U_H) = (\psi_k, 0)$ and $(P_H, U_H) = (0, \phi_k)$, respectively. These are, in fact, the so-called multiscale basis functions that we have described before in [1].
ii. Although not necessary, in this article each of the basis functions ψ_l and ϕ_ℓ that span $\mathcal{P}_H$ and $\mathcal{U}_H$ is chosen to have as support one single interface Γ_{ij} of the mesh skeleton Γ, greatly simplifying the system assembly and leading to a sparse matrix $\underline{\underline{A}}$. Moreover, such choice for the space $\mathcal{P}_H$ allows us to obtain a conservative solution at the coarse scale H for $\beta < +\infty$, a fact easily verified through expression (18).

3 The velocity postprocessing schemes

Let us recall that the multiscale solutions produced by the MRCM are mass-conserving at the coarse scale of the domain decomposition, i.e., for each interface Γ_{ij} between subdomains Ω_i and Ω_j, it holds

$$\int_{\Gamma_{ij}} \left(\mathbf{u}_h^i \cdot \check{\mathbf{n}} - \mathbf{u}_h^j \cdot \check{\mathbf{n}}\right) = 0,\ \forall\, i, j. \qquad (21)$$

The solution is, however, discontinuous at the fine level, except when the algorithmic parameter α is taken very large as we have illustrated (see Fig. 2). Some postprocessing or downscaling procedure on the velocity field becomes thus essential if transport of any quantity such as a fluid saturation or the concentration of a passive tracer is to be solved. A natural and simple way to deal with such discontinuous field is to take the average value of the two-sided solution at the interfaces between subdomains so as to define a unique flux on the fine grid over the skeleton of the domain decomposition. Given the multiscale solutions

$\mathbf{u}_h^i,\ i = 1, \ldots, N$, this amounts to computing in a first step for each Γ_{ij} a new interface field defined as

$$\overline{\mathbf{U}}_h^{ij} \doteq \frac{1}{2}\left(\mathbf{u}_h^i|_{\Gamma_{ij}} + \mathbf{u}_h^j|_{\Gamma_{ij}}\right). \tag{22}$$

Notice that the new velocity $\overline{\mathbf{U}}_h^{ij}$ transfers the same mass through the interfaces as the two-sided multiscale solution, i.e.,

$$\int_{\Gamma_{ij}} \mathbf{u}_h^i \cdot \check{\mathbf{n}} = \int_{\Gamma_{ij}} \mathbf{u}_h^j \cdot \check{\mathbf{n}} = \int_{\Gamma_{ij}} \overline{\mathbf{U}}_h^{ij} \cdot \check{\mathbf{n}}. \tag{23}$$

Once the flux values on every Γ_{ij} are updated, we proceed to the second step: for each subdomain Ω_i, solve

$$\begin{cases} \widetilde{\mathbf{u}}_h^i = -K\,\nabla \widetilde{p}_h^i & \text{in } \Omega_i, \\ \nabla \cdot \widetilde{\mathbf{u}}_h^i = f & \text{in } \Omega_i, \\ \widetilde{\mathbf{u}}_h^i \cdot \check{\mathbf{n}}^i = \mathbf{u}_h^i \cdot \check{\mathbf{n}}^i & \text{on } \partial\Omega_i \cap \partial\Omega, \\ \widetilde{\mathbf{u}}_h^i \cdot \check{\mathbf{n}}^i = \overline{\mathbf{U}}_h^{ik} \cdot \check{\mathbf{n}}^i & \text{on } \Gamma_{ik}, \forall k, \end{cases} \tag{24}$$

where index k above runs over all subdomains adjacent to Ω_i. After these two steps we end up with a flux field which is conservative on the fine grid and therefore suitable for transport. We refer to this method as the Mean method. Notice in (24) that along $\partial\Omega_i \cap \partial\Omega$ the original velocity multiscale solution is being imposed as boundary condition. This approach is quite simple to implement and relatively cheap. The only operation that involves some additional cost is the solution of subdomain problems (24), which can clearly be done in parallel.

The question considered here is whether alternative methods can be designed that have complexity similar to that of the Mean method while exhibiting better accuracy. The aim of this article is precisely to propose two new alternatives to the Mean method, namely, the Patch and the Stitch methods, which are now explained and later on assessed in the results section.

3.1 The Patch method

Let us consider oversampling regions around each interface Γ_{ij} covering the skeleton of the domain decomposition. These regions are called patches and they are made up of a collection of fine grid cells of the underlying discretization. In our implementation each one covers one single interface Γ_{ij} and has a thickness in the directions perpendicular to Γ_{ij} typically formed by 1 to 4 layers of fine cells, as illustrated in Fig. 4. Notice that these regions may intersect.

The idea is to solve local Darcy problems on these patches so as to define a unique velocity field on each interface Γ_{ij}. The procedure can be divided into three steps:

Step 1 - Patch problems: For each Γ_{ij} define a patch Ω_{ij} that encloses the interface, formed by a collection of fine grid elements of Ω_i and Ω_j and solve:

$$\begin{cases} \mathbf{u}_h^{ij} = -K\,\nabla p_h^{ij} & \text{in } \Omega_{ij} \\ \nabla \cdot \mathbf{u}_h^{ij} = f & \text{in } \Omega_{ij} \\ \mathbf{u}_h^{ij} \cdot \mathbf{n}_{ij} = \begin{cases} \mathbf{u}_h^i \cdot \mathbf{n}_{ij} & \text{if } \mathbf{x} \in \Omega_i \\ \mathbf{u}_h^j \cdot \mathbf{n}_{ij} & \text{if } \mathbf{x} \in \Omega_j \end{cases} & \text{on } \partial\Omega_{ij} \end{cases}, \tag{25}$$

where $\mathbf{n}_{ij}$ is the exterior normal vector to $\partial\Omega_{ij}$.

Step 2 - Restriction: For each interface define a new interface field as the restriction of $\mathbf{u}_h^{ij}$ to Γ_{ij}, i.e.,

$$\widetilde{\mathbf{U}}_h^{ij} \doteq \mathbf{u}_h^{ij}|_{\Gamma_{ij}}. \tag{26}$$

Step 3 - Subdomain problems: For each Ω_i, solve:

$$\begin{cases} \widetilde{\mathbf{u}}_h^i = -K\,\nabla \widetilde{p}_h^i & \text{in } \Omega_i, \\ \nabla \cdot \widetilde{\mathbf{u}}_h^i = f & \text{in } \Omega_i, \\ \widetilde{\mathbf{u}}_h^i \cdot \check{\mathbf{n}}^i = \mathbf{u}_h^i \cdot \check{\mathbf{n}}^i & \text{on } \partial\Omega_i \cap \partial\Omega, \\ \widetilde{\mathbf{u}}_h^i \cdot \check{\mathbf{n}}^i = \widetilde{\mathbf{U}}_h^{ik} \cdot \check{\mathbf{n}}^i & \text{on } \Gamma_{ik}, \forall k, \end{cases} \tag{27}$$

where index k above runs over all subdomains adjacent to Ω_i. This is exactly the same as in (24) with $\overline{\mathbf{U}}_h^{ij}$ replaced by $\widetilde{\mathbf{U}}_h^{ij}$. After steps 1–3, we end up with a mass-conserving flux field. The extension to three dimensions is straightforward. One can easily check that the new interface velocity satisfies

$$\int_{\Gamma_{ij}} \mathbf{u}_h^i \cdot \check{\mathbf{n}} = \int_{\Gamma_{ij}} \mathbf{u}_h^j \cdot \check{\mathbf{n}} = \int_{\Gamma_{ij}} \widetilde{\mathbf{U}}_h^{ij} \cdot \check{\mathbf{n}}, \tag{28}$$

since the solutions of the local problems are obtained by a mass-conserving method and satisfies the compatibility condition

$$\int_{\partial\Omega_{ij}} \mathbf{u}_h^{ij} \cdot \mathbf{n}_{ij} = \int_{\Omega_{ij}} f. \tag{29}$$

Also notice that problems (25) and (27) are undefined up to a pressure constant. The indeterminacy is in practice removed by imposing the average pressure field to be zero.

Interestingly, this method can be turned into an iterative scheme by repeating the process and taking in equation (25) (in **Step 1**) the last computed $\widetilde{\mathbf{u}}_h^i$ instead of the multiscale solution $\mathbf{u}_h^i$. A few iterations have shown to provide a more accurate result when compared to the fine grid solution, however, based on our numerical experimentation we have concluded the benefit brought by such iterative method does not justify the additional computational cost involved.

Fig. 4 The Patch method

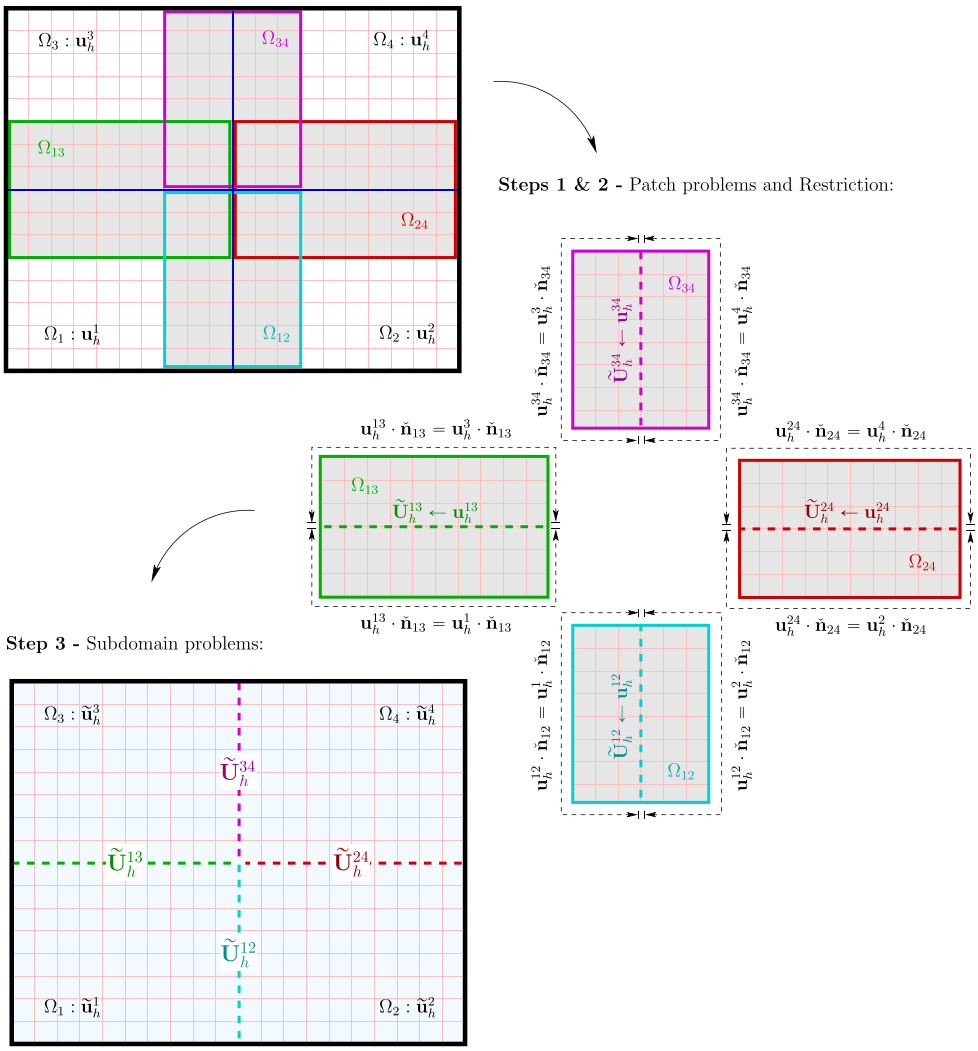

In the Mean method, the only necessary operation to define a unique flux at the interfaces is the averaging of the original multiscale flux solution, whereas in the Patch method this is accomplished by executing **Steps 1** and **2**, that obviously involve an additional cost. However, the local patch problems are small as compared to the subdomain problems, whose resolution is part of both methods and dominates the overall computational cost of the downscaling procedures. All these tasks can always be executed efficiently in parallel.

3.2 The Stitch method

We propose another method based on the idea of solving local problems on patches around the interfaces of the domain decomposition. Informally speaking, in this method, instead of recomputing the solutions over the subdomains, we simply "stitch" the local patch solutions to the global multiscale solution. In order to proceed we must first distinguish two situations: (i) Overlapping patches; and (ii) Non-overlapping patches. The first case, is the one to be adopted if using non-simplicial grids for discretization in the subdomains, as is the case in our implementation that uses rectangular Cartesian grids. The second case is feasible when using simplicial grids for discretization. These two situations are illustrated in Fig. 5.

Let us consider the first case of overlapping patches. In such case, in order to produce a mass-conserving solution, the local patches need to be separated into disjoint sets. This can in principle be done in an arbitrary way. In our implementation, for the sake of simplicity we separate into two sets: the sets of horizontal and vertical patches, as displayed in Fig. 6. In this case, the downscaling method proceeds as follows:

Step 1 - Horizontal patch problems: For each horizontal interface Γ_{ij} define a patch Ω_{ij}^{H} that encloses the

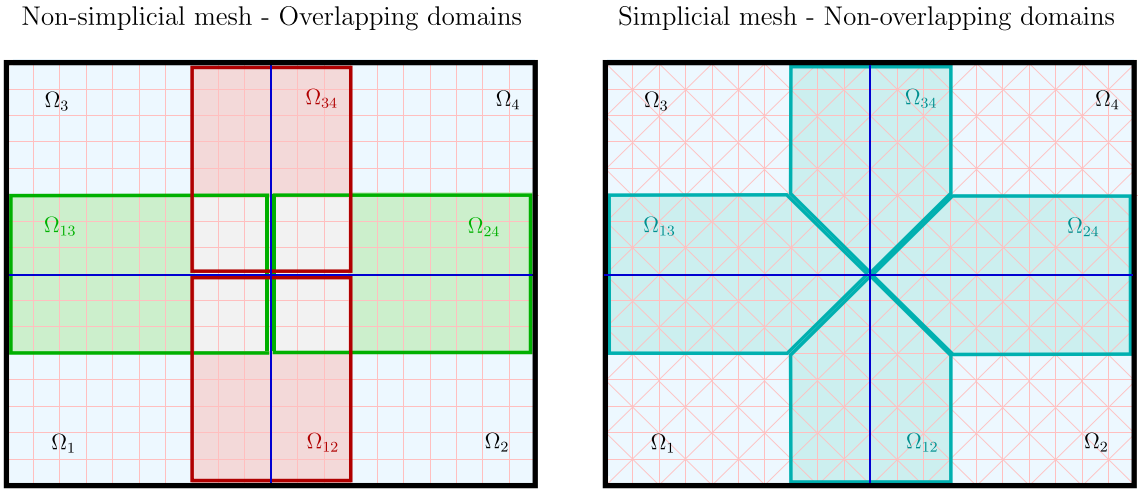

Fig. 5 Examples of patch definitions for the Stitch method. Overlapping domains with non-simplicial mesh (left) and non-overlapping domains with simplicial mesh (right)

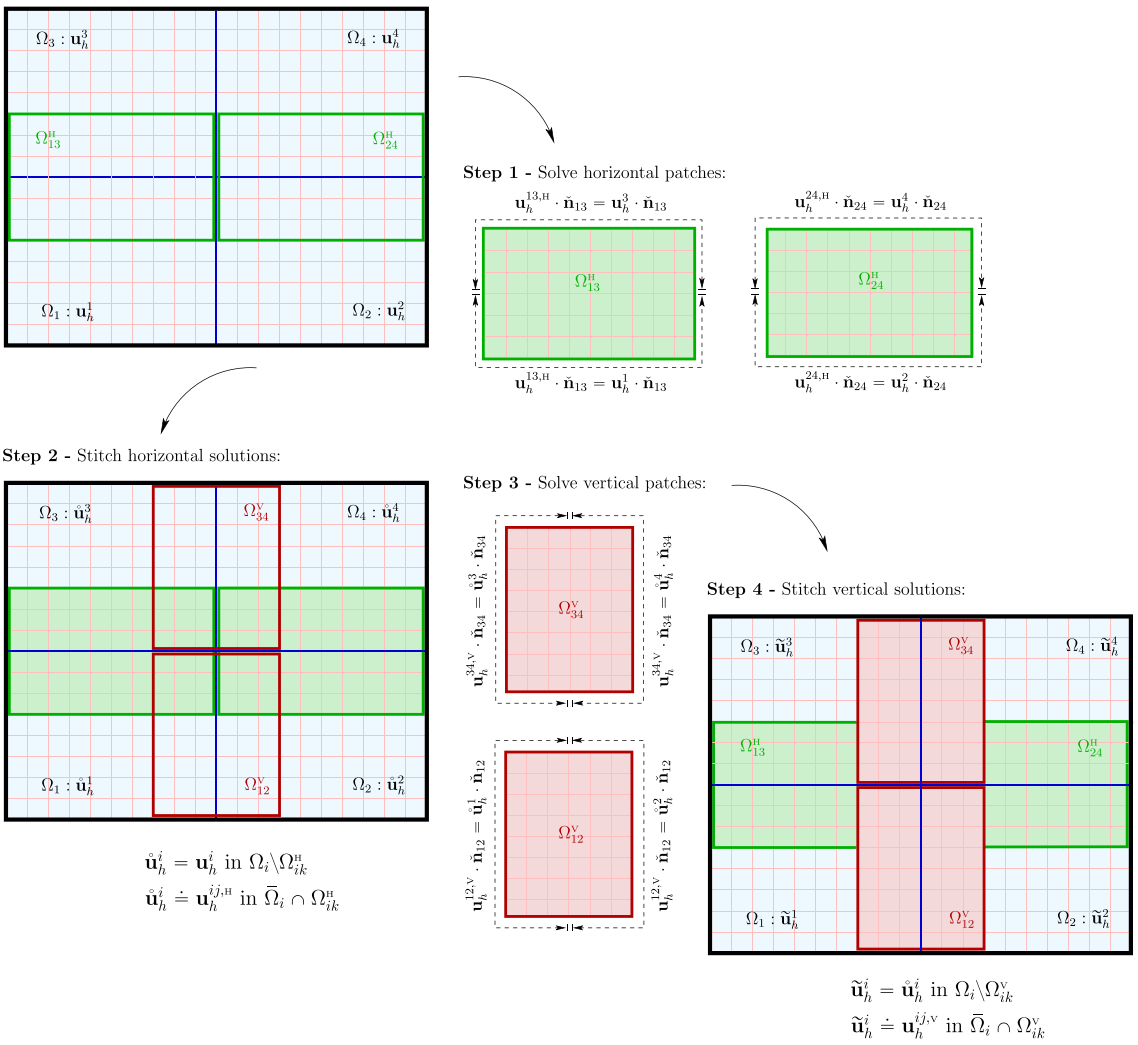

Fig. 6 The Stitch method

interface, formed by a collection of fine grid elements of Ω_i and Ω_j and solve:

$$\begin{cases} \mathbf{u}_h^{ij,\mathrm{H}} = -K\,\nabla p_h^{ij,\mathrm{H}} & \text{in } \Omega_{ij}^{\mathrm{H}} \\ \nabla\cdot\mathbf{u}_h^{ij,\mathrm{H}} = f & \text{in } \Omega_{ij}^{\mathrm{H}} \\ \mathbf{u}_h^{ij,\mathrm{H}}\cdot\mathbf{n}_{ij} = \begin{cases} \mathbf{u}_h^i\cdot\mathbf{n}_{ij} & \text{if } \mathbf{x}\in\Omega_i \\ \mathbf{u}_h^j\cdot\mathbf{n}_{ij} & \text{if } \mathbf{x}\in\Omega_j \end{cases} & \text{on } \partial\Omega_{ij}^{\mathrm{H}} \end{cases}, \tag{30}$$

where $\mathbf{n}_{ij}$ is exterior normal vector to $\partial\Omega_{ij}^{\mathrm{H}}$.

Step 2 - Stitch horizontal solutions: For each subdomain Ω_i, take:

$$\begin{aligned} \mathring{\mathbf{u}}_h^i &\doteq \mathbf{u}_h^i \text{ in } \Omega_i\backslash\Omega_{ik}^{\mathrm{H}}, \\ \mathring{\mathbf{u}}_h^i &\doteq \mathbf{u}_h^{ij,\mathrm{H}} \text{ in } \overline{\Omega}_i\cap\Omega_{ik}^{\mathrm{H}}, \forall k \end{aligned} \tag{31}$$

where index k runs over all horizontal patches that intersect with Ω_i.

Step 3 - Vertical patch problems: For each vertical interface Γ_{ij} define a patch Ω_{ij}^{V} that encloses the interface, formed by a collection of fine grid elements of Ω_i and Ω_j and solve:

$$\begin{cases} \mathbf{u}_h^{ij,\mathrm{V}} = -K\,\nabla p_h^{ij,\mathrm{V}} & \text{in } \Omega_{ij}^{\mathrm{V}} \\ \nabla\cdot\mathbf{u}_h^{ij,\mathrm{V}} = f & \text{in } \Omega_{ij}^{\mathrm{V}} \\ \mathbf{u}_h^{ij,\mathrm{V}}\cdot\mathbf{n}_{ij} = \begin{cases} \mathring{\mathbf{u}}_h^i\cdot\mathbf{n}_{ij} & \text{if } \mathbf{x}\in\Omega_i \\ \mathring{\mathbf{u}}_h^j\cdot\mathbf{n}_{ij} & \text{if } \mathbf{x}\in\Omega_j \end{cases} & \text{on } \partial\Omega_{ij}^{\mathrm{V}} \end{cases}, \tag{32}$$

Step 4 - Stitch vertical solutions: For each subdomain Ω_i, take:

$$\begin{aligned} \widetilde{\mathbf{u}}_h^i &\doteq \mathring{\mathbf{u}}_h^i \text{ in } \Omega_i\backslash\Omega_{ik}^{\mathrm{V}}, \\ \widetilde{\mathbf{u}}_h^i &\doteq \mathbf{u}_h^{ij,\mathrm{V}} \text{ in } \overline{\Omega}_i\cap\Omega_{ik}^{\mathrm{V}}, \forall k \end{aligned} \tag{33}$$

where index k runs over all vertical patches that intersect with Ω_i. After steps 1–4 we end up with a velocity field $\widetilde{\mathbf{u}}_h^i$ which is mass-conserving on the fine grid and continuous at subdomain interfaces. The extension to three dimensions is straightforward.

In the second aforementioned situation of non-overlapping patches the computation can be done all at once, i.e., in a first step all patches are solved simultaneously and, in a second step, the solutions are stitched in order to produce a mass-conserving global solution. This last case has not been implemented and its assessment is left for future works.

This method is the most attractive one in regards to computational cost, since it does not require solution of the subdomain problems, but only resolution of local small patch problems around the interfaces.

Before passing to the numerical results, we summarize the computational effort involved in the abovementioned postprocessing schemes. This is given in Table 1 where all considered methods were grouped into three main tasks that dominate the computational cost in the schemes. In this table e stands for the number of fine grid elements defining the thickness of the patch problems around the interfaces and N_f is the number of fine grid elements contained per interface.

4 Numerical setup

In order to compare the downscaling schemes under the same conditions we consider the transport of a passive tracer in highly heterogeneous permeability fields $K(\mathbf{x})$. Two types of absolute permeability fields are considered here, the first being the log-normal, $K(\mathbf{x}) = \exp(\gamma\xi(\mathbf{x}))$, in which $\xi(\mathbf{x})$ is a Gaussian field and γ a constant value chosen that controls the contrast, i.e., $K_{\max}/K_{\min}$. Here, $\xi(\mathbf{x})$ is characterized by its mean value μ_ξ and an exponential anisotropic covariance function given by

$$C_\xi(\mathbf{r}) = \sigma_\xi^2 e^{-d(\mathbf{r})},$$

where σ_ξ is a constant variance and $d(\mathbf{r}) = \sqrt{r_1^2/I_x + r_2^2/I_y}$ with I_x and I_y being correlation lengths and r_1 and r_2 the two-point separation distance in longitudinal and transverse direction, respectively. To generate these log-conductivity fields we have used the Hydro-Gen package [12]. The second type considered are the layers of the SPE10 project [13] that is highly heterogeneous and presents channelized structures.

In all the numerical experiments the domain is a 2D region $\Omega = [0, L_x]\times[0, L_y]$. For the Darcy problem no-flow boundary conditions are considered at $y = 0$ and $y = L_y$ and inflow-outflow boundary conditions are imposed at $x = 0$ and $x = L_x$, respectively.

For the MRCM we have considered piecewise polynomial functions both for the pressure space $\mathcal{P}_H$ and for the flux space $\mathcal{U}_H$. In fact, we use elementwise constant

Table 1 Involved tasks and related computational effort of the postprocessing schemes

Task	Comp. effort	Mean	Patch	Stitch
Patch prob.	4 prob. of size $N_f\times(2\,e)$	–	Eq. 25	Eqs. (30)–(32)
Unique flux	Negligible	Eq. (22)	Eq. (26)	Eqs. (31)–(33)
Local prob.	1 local prob. of size N_f^2	Eq. (24)	Eq. (27)	–

fine grid representation of polynomials over the interface elements

$$\mathcal{U}_H = \{V_H,\ V_H|_e = \Pi_0(q), q \in \mathbb{P}_{k_U-1}(e),\ e \in \mathcal{T}_H\},$$
$$\mathcal{P}_H = \{M_H,\ M_H|_e = \Pi_0(q), q \in \mathbb{P}_{k_P-1}(e),\ e \in \mathcal{T}_H\},$$

where $\mathbb{P}_l$, is the space of polynomials of degree $\leq l$ and Π_0 is the L^2–projection of a function $\mathbb{P}_l(e)$ onto the space $F_h(e),\ e \in \mathcal{T}_H$. In the numerical results section the experiments are performed by choosing a total number of degrees of freedom per interface $k = k_U + k_P$. Although not mandatory, this number will be the same for all interfaces. Also, for simplicity, the number of fine grid elements per interface N_f is chosen to be the same for all interfaces. In such case the order reduction obtained by our multiscale method is simply computed as $(N_f - k)/N_f$, where order reduction stands for the number of unknowns being used to couple the local multiscale basis functions compared to the number of unknowns to be solved by a standard non-overlapping domain decomposition method such as the ones proposed in [14, 15].

For the transport problem we assume a water saturated field ($\mathcal{C}(\mathbf{x}, t_0) = 0, \mathbf{x} \in \Omega$) with a passive tracer injected on $x = 0$ at time $t = t_0$, carried by the flow for $t > t_0$. In order to solve the transport equation a classical upwind scheme combined with a TVD Runge-Kutta of second order in time is adopted for discretization. Let us provide some details about the scheme. Given the fine grid partition $\mathcal{T}_h$ of Ω, a cell-centered finite volume conservative scheme is considered for the concentration unknowns. For each fine grid element of $\mathcal{T}_h$, $V_i,\ i = 1, \ldots, m$, the discrete concentration field $\mathcal{C}_h$ satisfies

$$\frac{d}{dt}\int_{V_i} \mathcal{C}_h\, dV = -\sum_{E \in \partial V_i} \int_E \mathcal{C}_h|_E\, \widetilde{\mathbf{u}}_h \cdot \boldsymbol{\nu}\, dS, \tag{34}$$

where $\widetilde{\mathbf{u}}_h$ is the postprocessed multiscale velocity field, which is already given at the edges of V_i and $\boldsymbol{\nu}$ is the outer normal to ∂V_i. As mentioned, for the edge concentration $\mathcal{C}_h|_E$ the upwind value is taken. This leads to the semi-discrete system

$$\frac{d}{dt}\underline{C} = \mathcal{F}(\underline{C}),$$

where $\underline{C} \in \mathbb{R}^m$ and $C_i = \frac{1}{|V_i|}\int_{V_i} \mathcal{C}_h\, dV$. Applying a TVD Runge-Kutta scheme of second order ([16]) a fully discrete system is obtained. Defining the time step δt, the unknown vector at time level $n+1$ is obtained from

$$\underline{C}^{(n+1)} = \frac{1}{2}\underline{C}^n + \frac{1}{2}\underline{C}^* + \frac{1}{2}\,\delta t\, \mathcal{F}(\underline{C}^*), \tag{35}$$

where

$$\underline{C}^* = \underline{C}^n + \delta t\, \mathcal{F}(\underline{C}^n). \tag{36}$$

5 Numerical results

We begin this section by assessing the coupling between the multiscale solution of the MRCM and the postprocessing schemes. Two types of domain decomposition are considered in combination with different interface spaces. These results allow us to define the MRCM parameters and evaluate the error produced by increasing the size of the patches in the postprocessing schemes. Based on these results, we choose a patch size and repeat the previous experiment for a collection of permeability fields with the same covariance function as well as for permeability fields taken from the SPE10 project. From these we obtain some metrics for the error of the schemes. Finally, we evaluate the error and the convergence order of downscaling schemes coupled with the MMMFEM, the MHM, and the MRCM with enriched interface spaces for permeability fields with and without channel structures.

In this section the downscaling methods are assessed in terms of the $L^2(\Omega)$ relative error norm of the tracer concentration, defined as

$$E_c(\tilde{t}) = \frac{\|\mathcal{C}_{msc}(\mathbf{x}, \tilde{t}) - \mathcal{C}_{fine}(\mathbf{x}, \tilde{t})\|_{L^2(\Omega)}}{\|\mathcal{C}_{fine}(\mathbf{x}, \tilde{t})\|_{L^2(\Omega)}},$$

in which $\mathcal{C}_{msc}(\mathbf{x}, t)$ is the result obtained by using the postprocessed flux multiscale solution and $\mathcal{C}_{fine}(\mathbf{x}, t)$ is the result obtained by using the fine grid flux solution.

5.1 First approach

We start by considering a domain Ω with dimensions $L_x = L_y = 1$ and square fine elements of size $h = 1/120$. For the absolute permeability field $K(\mathbf{x}) = \exp(\gamma\xi(\mathbf{x}))$, we set $\xi(\mathbf{x})$ with $I_x = 5 \times h$, $I_y = 12 \times h$, $\mu_\xi = 0$ and $\sigma_\xi = 1$ and take $\gamma = 2$, leading to a contrast of order $K_{max}/K_{min} \simeq 10^6$. The domain is decomposed into 4×4 and 8×8 square subdomains of size $H = 30h$ and $H = 15h$, respectively. For the interface spaces we have considered $k = 2, 3, 4$. Table 2 displays the order reduction obtained by the multiscale method for the above cases.

The degrees of freedom (*dof's*) are distributed in the possible combinations such that $k_P + k_U = k$ and the patches' thicknesses are taken as two fine elements in the

Table 2 Order reduction for the multiscale solutions of the first numerical experiment

	No. of dof's per interface k		
	2	3	4
4×4	93.3%	90.0%	86.7%
8×8	86.7%	80.0%	73.3%

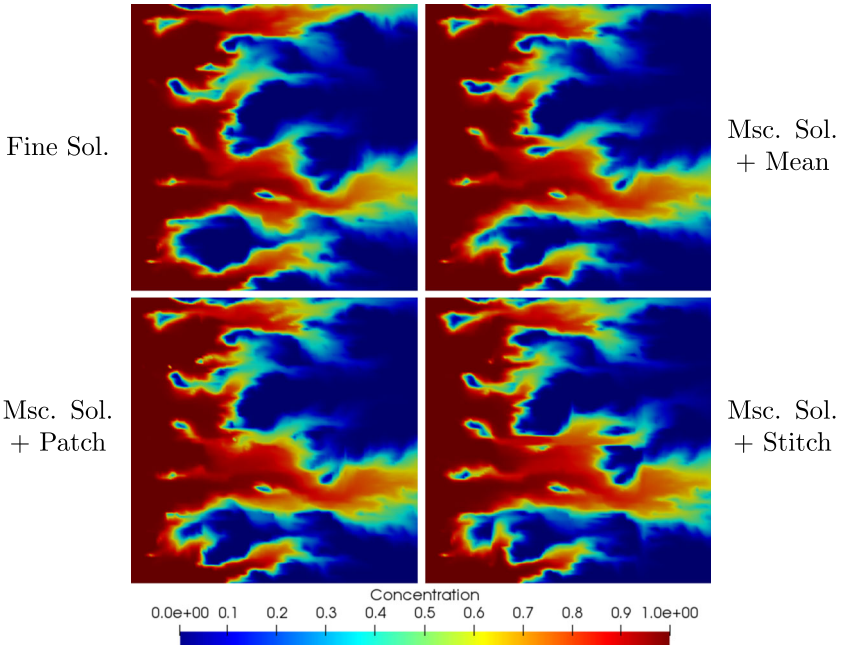

Fig. 7 Concentration at time $t = 0.5$ for the fine solution and multiscale solution with $k = 2$

downscaling schemes. The transport equation is solved with $\delta t = 10^{-5}$, that satisfies a CFL condition for all the problems considered here, from $t_0 = 0$ to $t_{MAX} = 1$. Figure 7 displays the concentration transported by the fine solution and the concentration transported by the multiscale solution with $k = 2$ and the downscaling schemes at time $t = 0.5$ for the 4×4 decomposition. The relative errors from t_0 to t_{MAX} are shown in Fig. 8.

One can note in the considered cases that the Patch scheme consistently has the smallest errors when compared to the other two schemes. Also, the Stitch scheme presents larger errors when the multiscale method has $k_P = k_U = 1$ for the 4×4 domain decomposition and $k_U > k_P$ and presents similar errors to the Mean scheme in all other cases.

From our experience, the precision of the postprocessing schemes depends on the accuracy of the multiscale solution. With this observed we set the MRCM with $k_P = k_U = 2$ and a 4×4 domain decomposition, where the schemes have similar errors and the multiscale solution has a reduced computational cost, to further assess the downscaling schemes.

Now we evaluate the impact of the patch thickness on the error of the Patch and Stitch schemes. We take the problem defined above and increase the thickness from 2 fine elements to 10 fine elements. Results are shown in Fig. 9.

Larger patches lead to smaller errors in both schemes, but the gain in accuracy is not significant after about 6 fine elements. To keep the patch problems small relative to the subdomain problems, we set patches with 4 elements.

Figure 10 displays the relative error of the flux field for the multiscale solution and the relative errors after the postprocessing schemes. As is well known, multiscale methods based on non-overlapping domain decomposition have larger errors at the interfaces between subdomains, where the coupling is done through low order spaces, as shown in the left top of Fig. 10. From this experiment we observed that the Mean scheme, despite generating a continuous field, maintains existing errors at the interfaces. The scenario is different for the Patch and Stitch schemes, in which the patches include information from within the subdomains. The errors are greatly reduced at the interfaces and only remain concentrated at the corners of the domain decomposition as shown in Fig. 10.

5.2 Robustness

To check the robustness of the downscaling schemes we generate new log-conductivity fields, $\xi_j(\mathbf{x})$, $j = 1, \ldots, 100$, with the same properties described in the last section for different seeds, thus generating fields with similar structures distributed in spatially distinct patterns. With that we define new permeability fields $K_j(\mathbf{x})$, also taking $\gamma = 2$ and redo the last experiment from the previous section for each $j = 1, \ldots, 100$. In Fig. 11, we show some examples of these fields.

Figure 12 displays the mean error of all these simulations for each time t as well as the maximum and minimum errors and the maximum standard deviation over all the time steps.

The Patch scheme still displays smaller errors than the other two schemes for all errors measures. Similar errors in average for the Stitch and the Mean schemes are observed, although the Stitch has larger maximum errors and a

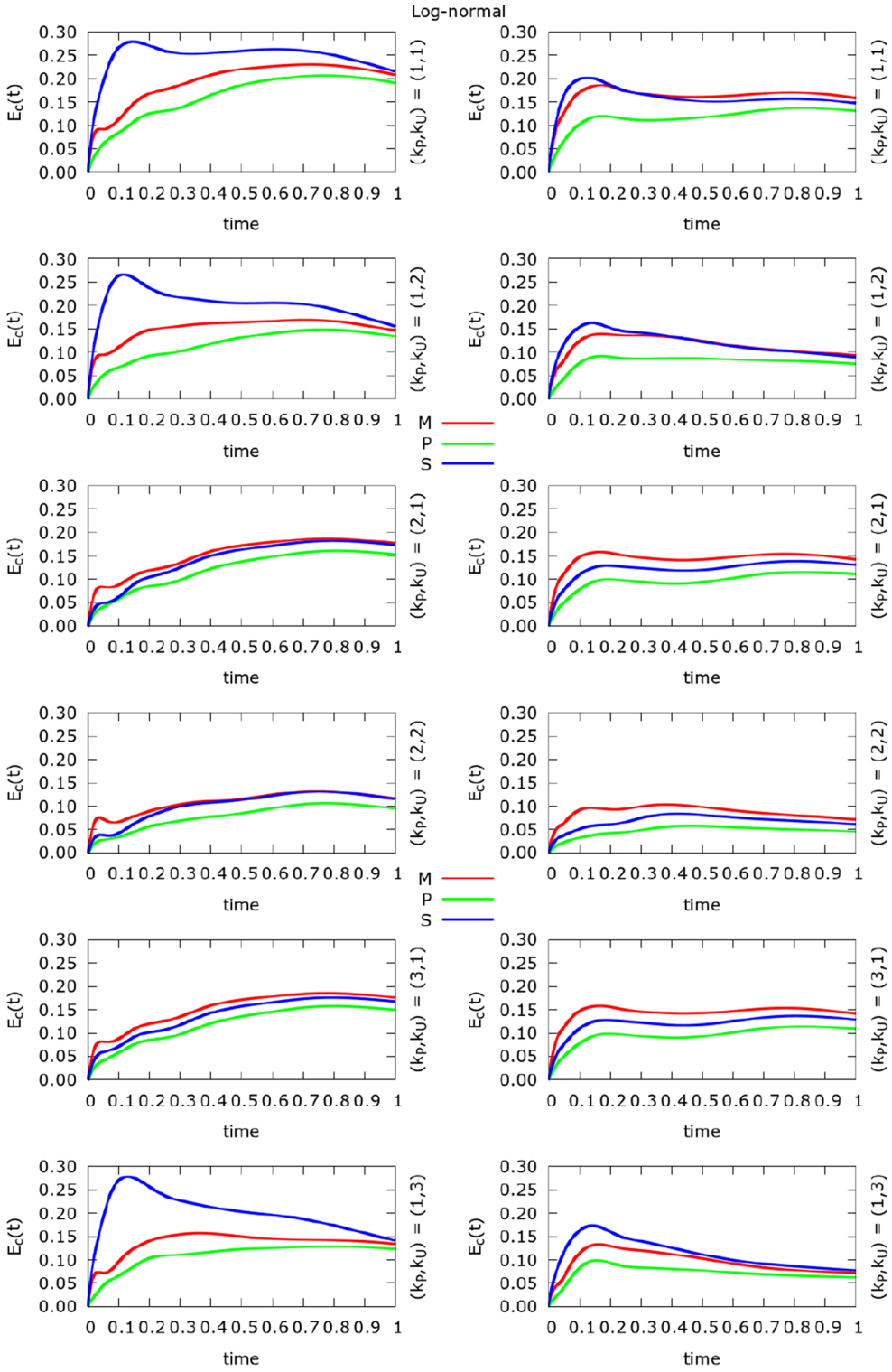

Fig. 8 Relative concentration errors for $k = 2, 3, 4$ and two domain decomposition: 4×4 (left column) and 8×8 (right column) for the downscaling schemes, the Mean (red line), the Patch (green line) and the Stitch (blue line)

standard deviation almost 1.5 times larger than the other schemes.

For the next numerical experiment, we take 2D layers of the SPE10 project [13] as permeability fields in a rectangular domain with dimensions $L_x = 11/3$ and $L_y = 1$. There are 85 highly heterogeneous layers in the SPE10 project. Layers 1 to 35 have structures similar to those of the fields previously explored and layers 36 to 85 have high correlation channels that pose realistic challenges and are commonly used for the evaluation of numerical methods in oil reservoir simulation. In Fig. 13 we show two examples of these layers, with and without channel structures.

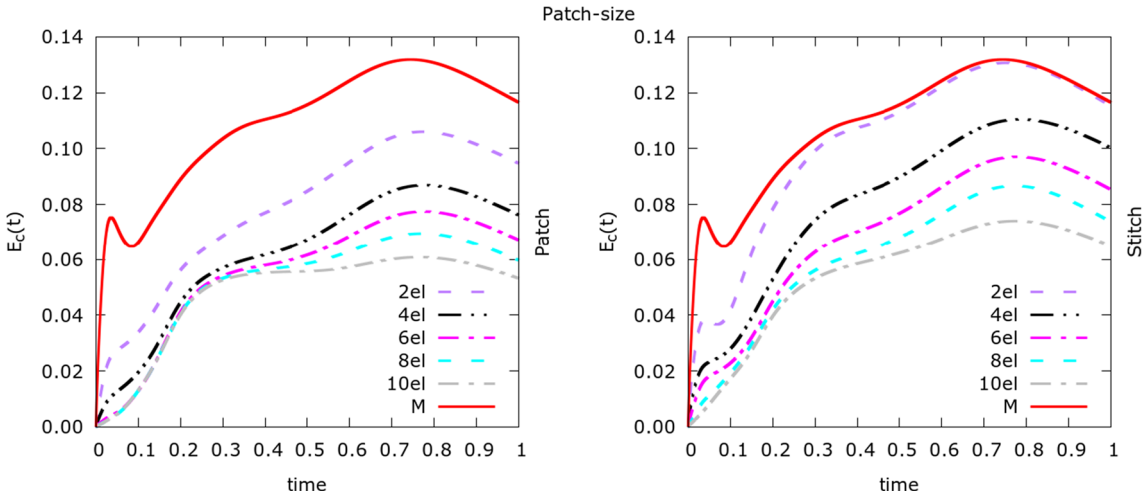

Fig. 9 Relative errors of the Patch (left) and the Stitch (right) for different patch thicknesses and the relative error of the Mean scheme (red line)

These fields are defined in a fine mesh with 220 × 60 elements. For the multiscale method, the domain is decomposed into 11 × 3 subdomains, each one with a fine mesh of 20 × 20 square elements of size $h = 1/60$. In this case the order reduction of the multiscale method is 80%. Figure 14 shows the solution of the transport equation at the breakthrough time for the fine solution and for the multiscale solution with the Stitch scheme. Figure 15 shows the maximum relative error among all time steps, t_o to t_{MAX} for each layer.

By looking at the concentration error it is easy to note the transition from layers without channels, where errors stay between 5 and 10%, to layers with channels, where errors range from 10 to 30%, as displayed in Fig. 15. For the downscaling schemes, the Patch method shows the smallest errors and the Stitch method provides intermediate errors between the Patch and Mean for all layers, although the errors for layers with channelized structures are similar. In Table 3 we show the mean error and the standard deviation for the cases with and without channels.

5.3 An example with wells

The accurate numerical description of the flow close to wells, source and sink terms in our context, is one of the major challenges related to multiscale approximations [17]. Such an issue is handled in a natural manner by

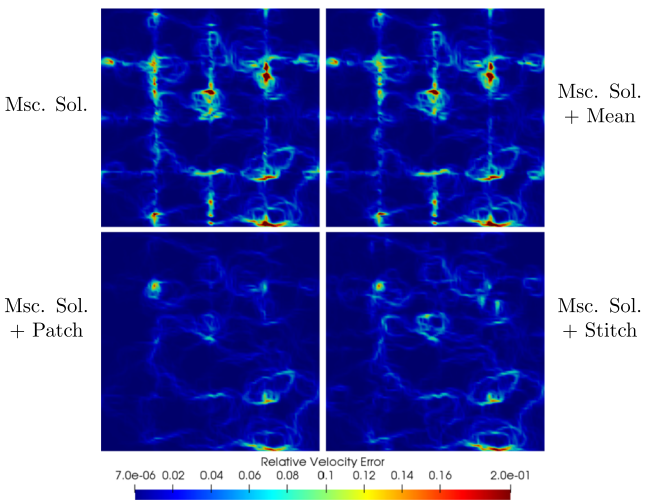

Fig. 10 Relative velocity field error to the maximum absolute velocity value of the fine solution w/o downscaling

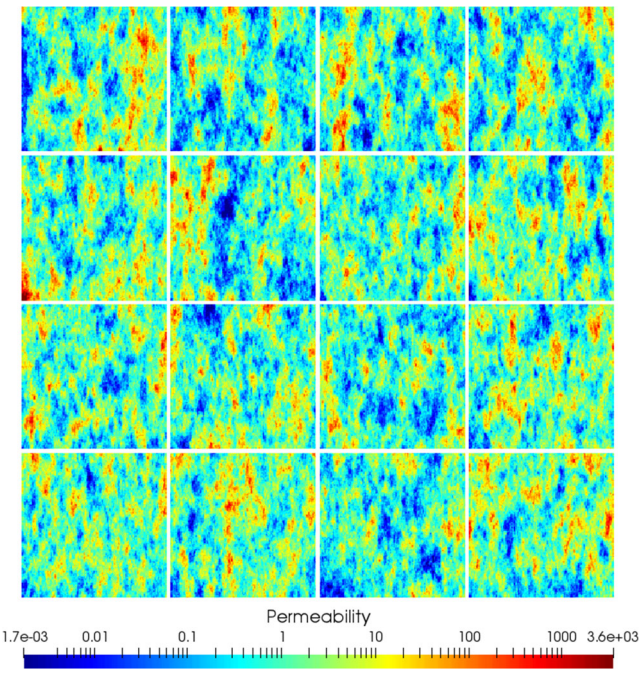

Fig. 11 Examples of permeability fields generated by the log-conductivity functions with different seeds

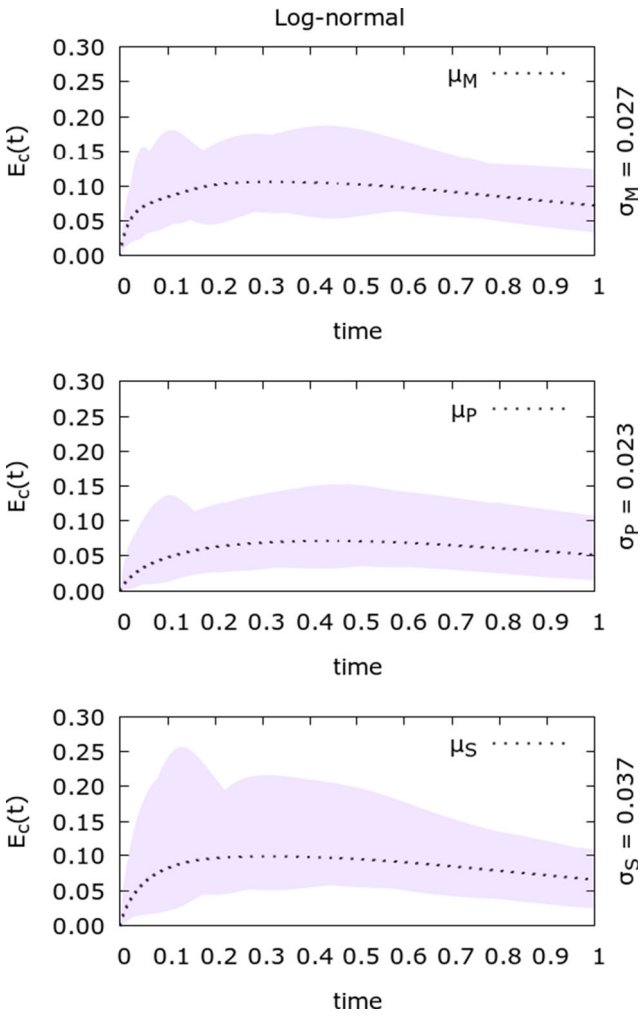

Fig. 12 Relative mean error μ at each time t for the permeability fields $K_j(\mathbf{x})$, $j = 1, \ldots, 100$, and the maximum standard deviation σ over t. Shaded area denotes the maximum and minimum error region

the MRCM as the effects of these terms are taking into account by computing a separate basis function via an additive decomposition of the global solution (see [1]). In this numerical experiment we evaluate the effect of the postprocessing schemes in this scenario. By defining layer 36 of the SPE10 project as the absolute permeability field with same mesh and domain decomposition as the previous examples, we set no-flow boundary condition in $\partial\Omega$ and define a set of sources and sinks compatible with the boundary conditions, i.e.,

$$\int_{\partial\Omega} \mathbf{u}_h \cdot \mathbf{n} = \int_{\Omega} f = 0. \tag{37}$$

For this example, we have slightly changed Eq. (34) in order to consider tracer sources. Figure 16 shows how the point sources and sinks are distributed over domain Ω. We have included the sinks (red squares) inside the patch regions, a setup not considered on the previous experiments. In Fig. 17 we display the velocity error relative to the maximum absolute velocity of the fine grid solution for the multiscale velocity field with and without the postprocessing schemes. Notice that the highest errors are related to the domain decomposition and to the high permeability channel than to near regions with sources and sinks.

In Fig. 18, we display the concentration profile at time $t = 1.0$ for the fine solution and the multiscale solution with the postprocessing schemes. The concentration error relative to the fine solutions are 14.2%, 6.8%, and 9.5% for the Mean, Patch and Stitch methods, respectively.

5.4 Comparison of multiscale methods

As mentioned earlier, the MRCM generalizes a family of multiscale methods and among them are the MMMFEM ($\beta = 0$) and the MHM ($\beta \to +\infty$). Taking advantage of this fact, we now compare the concentration errors of the postprocessing schemes when combined with the above multiscale methods for a collection of k values. From these results we will estimate a convergence order of the schemes when combined with these multiscale methods. Although the MHM multiscale solution has naturally a continuous

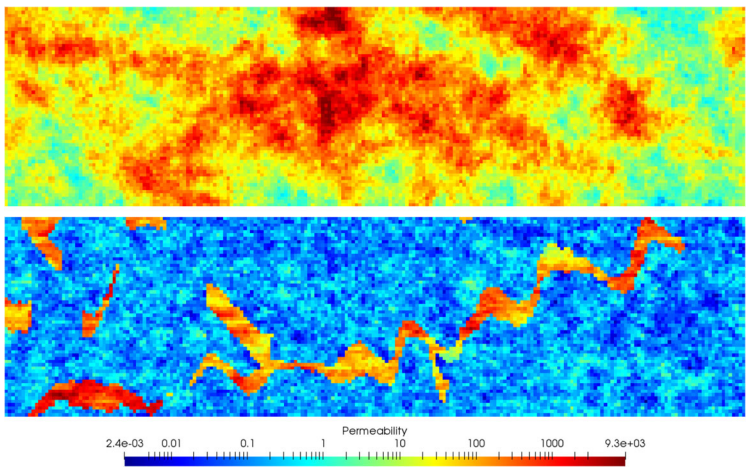

Fig. 13 Examples of permeability fields from SPE10 project: layer 20 (top) and layer 36 (bottom)

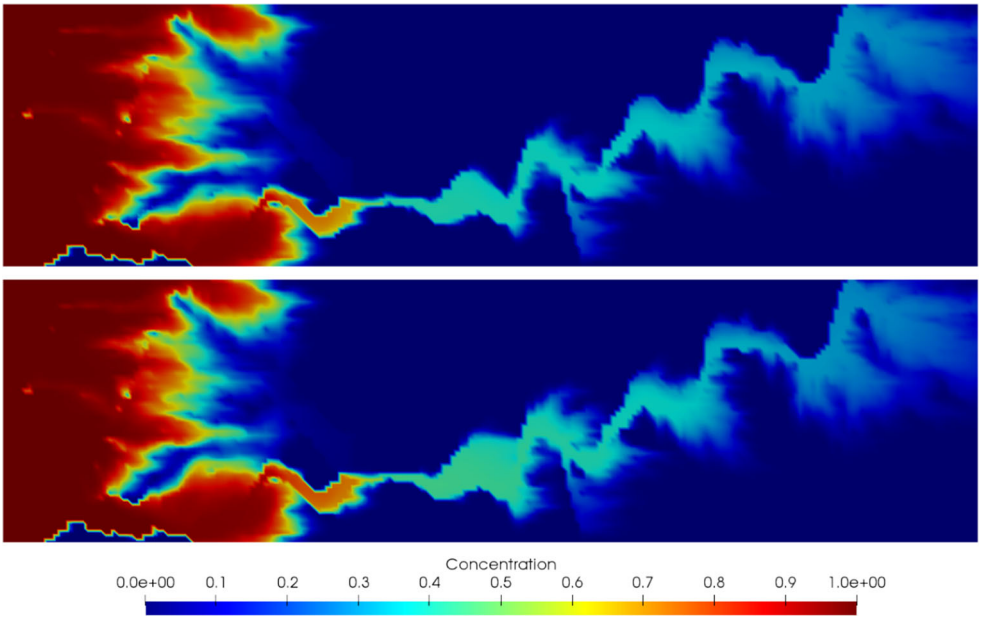

Fig. 14 Concentrations at breakthrough time for the fine solution (top) and the multiscale solution with $k = 4$ and the Stitch scheme (bottom) for layer 36

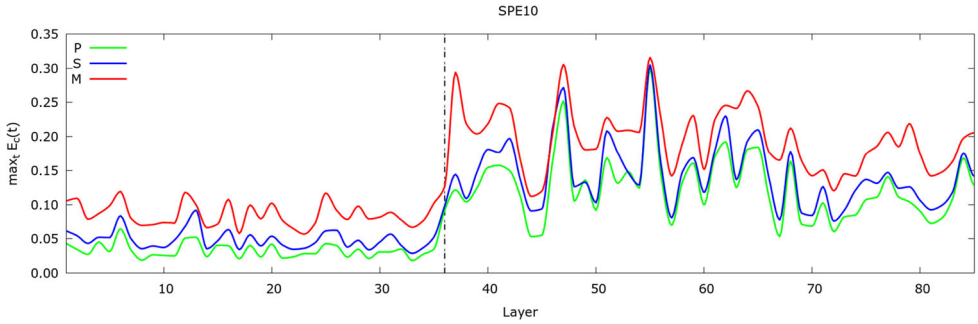

Fig. 15 Maximum relative error over t of the downscaling schemes, the Mean (red line), the Patch (green line), and the Stitch (blue line) for all layers of the SPE10 project. The dashed line indicates where the layers with channels begins

Table 3 Mean μ errors and the standard deviation σ of the SPE10 layers

	Layers ≤ 35		Layers ≥ 36	
	μ	σ	μ	σ
Patch	0.0330	0.0104	0.1245	0.0479
Stitch	0.0488	0.0137	0.1438	0.0486
Mean	0.0855	0.0170	0.1958	0.0467

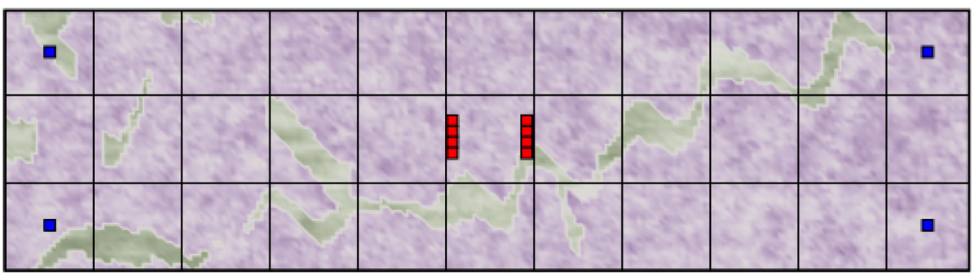

Fig. 16 Sources (blue squares) and sinks (red squares) distribution over the domain decomposition of Ω. The sinks are include inside the patch regions

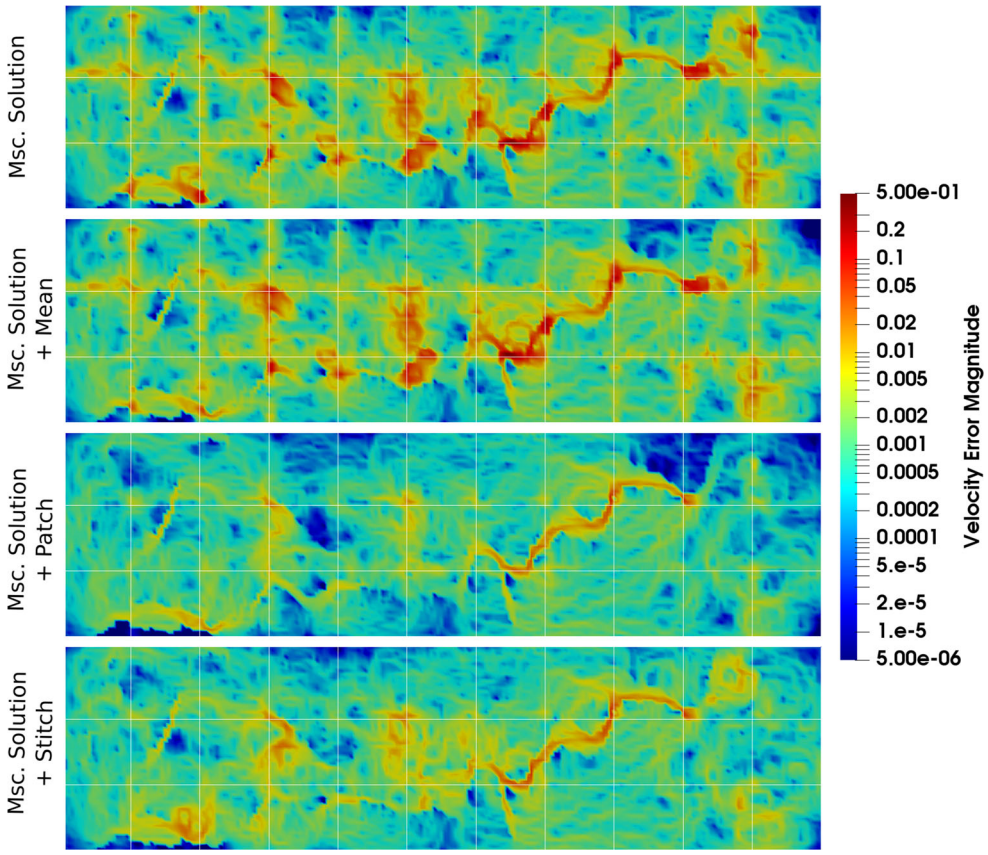

Fig. 17 Velocity error relative to the absolute maximum velocity of the fine grid solution. From top to bottom: multiscale solution, multiscale solution+Mean method, multiscale solution+Patch method and multiscale solution+Stitch method

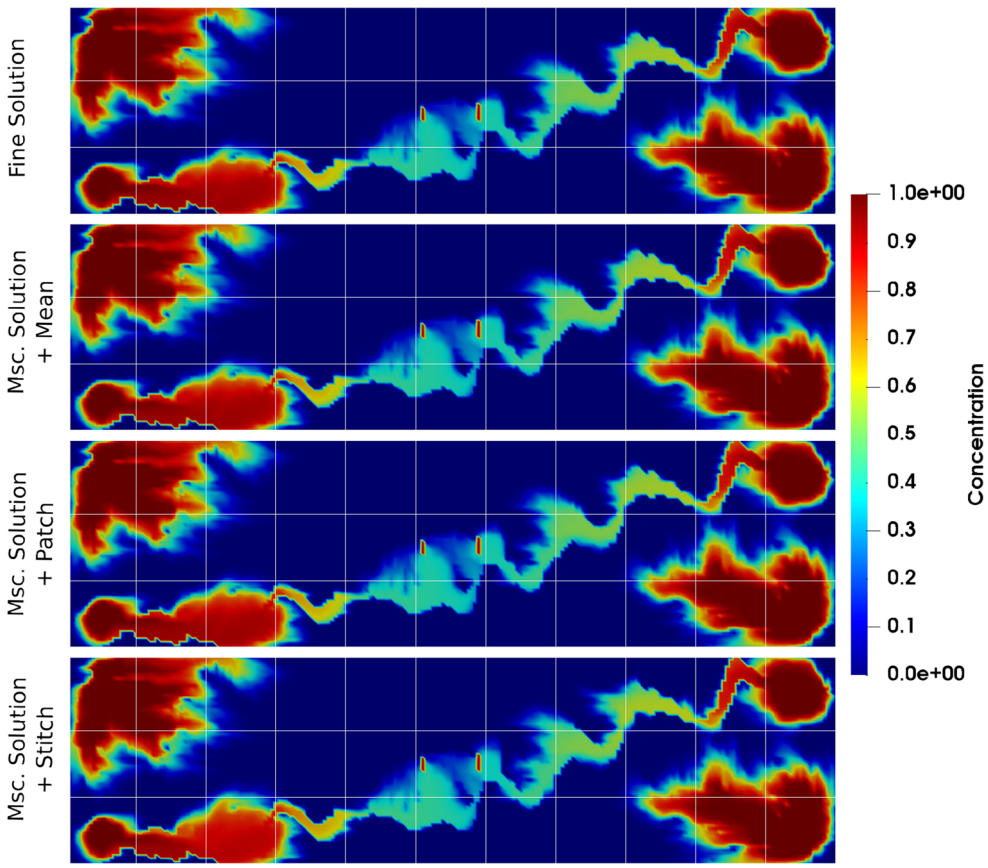

Fig. 18 Concentration profile at time $t = 1.0$. From top to bottom: fine solution, multiscale solution + Mean method ($E_c = 14.2\%$), multiscale solution + Patch method ($E_c = 6.8\%$) and multiscale solution + Stitch method ($E_c = 9.5\%$)

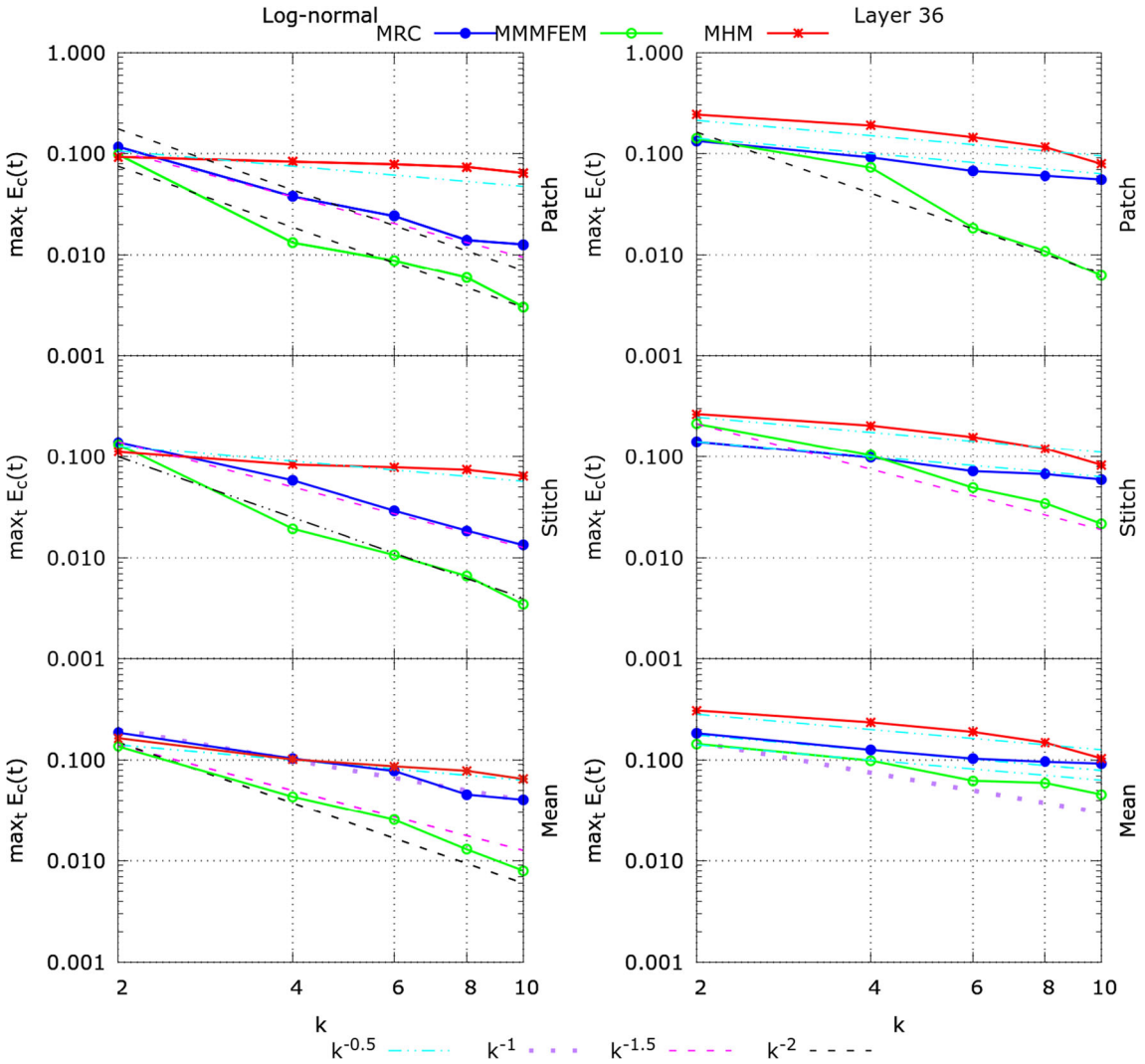

Fig. 19 Maximum relative errors over time t of the MRCM, MMMFEM and MHM for the log-normal field (left column) and the Layer 36 (right column) for enriched interface spaces

flux field without the need of a postprocessing scheme, we apply them in order to assess whether there is an improvement in terms of accuracy. Note that the Mean scheme does not change the MHM multiscale solution.

For the MRCM, we choose to keep the equidistribution of degrees of freedom between pressure and flux interface spaces, i.e., if we take $k = 4$, both pressure and flux interface spaces have linear functions per interface. On the other hand, the MMMFEM and the MHM with $k = 4$ are defined with cubic functions by interfaces in the pressure interface space and in the flux interface space, respectively. The experiment is performed using two types of permeability fields. For the first we use $\xi(x)$ with $\gamma = 2$ to define the permeability field $K(\mathbf{x}) = \exp(\gamma\xi(\mathbf{x}))$ in $\Omega = [0, 1]\times[0, 1]$ decomposed into 8×8 subdomains, each subdomain with a fine mesh of 15×15 square elements of size $h = 1/120$. For the second type, we take layer 36 of the SPE10 project and use the same configuration as the last experiment of the previous section.

Figure 19 shows the maximum concentration error over time from $k = 2$ until $k = 10$ for the above permeability fields. Table 4 displays the order reduction obtained by the multiscale methods.

For the log-normal field (left column on Fig. 19), the smallest errors are obtained by the MMMFEM with all

Table 4 Order reduction obtained by the multiscale method by enriching the interface spaces

	No. of dof's per interface k				
	2	4	6	8	10
Log-normal	86.7%	73.3%	60.0%	46.7%	33.3%
Layer 36	90.0%	80.0%	70.0%	60.0%	50.0%

Table 5 Convergence order on concentration for the multiscale methods in two types of permeability fields

	Log-normal			Layer 36		
	Patch	Stitch	Mean	Patch	Stitch	Mean
MRCM	$\mathcal{O}(k^{-1.5})$	$\mathcal{O}(k^{-1.5})$	$\mathcal{O}(k^{-1.0})$	$\mathcal{O}(k^{-0.5})$	$\mathcal{O}(k^{-0.5})$	$\mathcal{O}(k^{-0.5})$
MMMFEM	$\mathcal{O}(k^{-2})$	$\mathcal{O}(k^{-2.0})$	$\mathcal{O}(k^{-1.5})$	$\mathcal{O}(k^{-2.0})$	$\mathcal{O}(k^{-1.5})$	$\mathcal{O}(k^{-0.5})$
MHM	$\mathcal{O}(k^{-0.5})$	$\mathcal{O}(k^{-0.5})$	$\mathcal{O}(k^{-0.5})$	$\mathcal{O}(k^{-0.5})$	$\mathcal{O}(k^{-0.5})$	$\mathcal{O}(k^{-0.5})$

the downscaling schemes followed by the MRCM, with similar errors for $k = 2$ in all multiscale methods. In this type of permeability field, the MMMFEM shows a quadratic convergence order when combined with the Patch and Stitch schemes that drops to 1.5 when combined with the Mean scheme. On the other hand, the MRCM shows a 1.5 convergence order when combined with the Patch and Stitch schemes that drops to linear when combined with the Mean scheme and the MHM shows a convergence order of 0.5 when combined with all the downscaling schemes.

For layer 36 (right column of Fig. 19), the MMMFEM shows a quadratic numerical convergence when combined with the Patch scheme, that drops to 1.5 with the Stitch scheme and again drops to 0.5 when combined with the Mean scheme. The convergence order for the MRCM drops to 0.5 in combination with all the downscaling schemes, the same convergence order obtained for the MHM. A summary of convergence orders are depicted in Table 5.

6 Conclusions

We have started by recalling the main ingredients and implementation aspects of the recently proposed multiscale Robin coupled method (MRCM). After that, we have proposed two postprocessing methods to recover mass-conserving velocity fields from multiscale solutions that are only conservative in coarse scales. The new methods were compared with a standard method of the literature in terms of accuracy of the transport of contaminant in subsurface. Two types of very heterogeneous permeability fields were considered, the ones generated with the Hydro-Gen package and the fields given by the SPE10 project. Initially, the comparison was carried out with solutions produced by the MRCM with a set of predefined parameters. Thereafter, by suitable choices of the parameter β, we have compared the performance of the postprocessing procedures with solutions produced by the MMMFEM, the MRCM and the MHM with the same order reduction.

The numerical results indicate that the Patch method consistently has the smallest errors, followed by the Stitch method (which is the least expensive of the three) and then the Mean method. These results were very robust for the two types of permeability fields considered and for problems with and without wells. Furthermore, the new methods have reduced the velocity error at subdomain interfaces of the multiscale approximations, a task not accomplished by the Mean method.

Combining the Patch method with the MMMFEM proved to be the most accurate procedure in channelized fields, although significant differences in accuracy with other postprocessing schemes were only attained for multiscale solutions with order reduction less than or equal to 65%. In the more interesting cases with order reduction above 75% the Stitch method provides comparable accuracy and thus provides the best compromise between computational cost and precision.

Funding information This work received financial support from São Paulo Research Foundation FAPESP, grant 2013/07375-0, Cepid-CeMEAI, from the Brazilian National Council for Scientific and Technological Development (CNPq), and from the Brazilian oil company Petrobras. FSS is also funded by FAPESP grants 2016/08115-0 and 2015/02649-0. FP was also funded in part by NSF-DMS 1514808, a Science Without Borders/CNPq-Brazil grant and UT Dallas.

References

1. Guiraldello, R.T., Ausas, R.F., Sousa, F.S., Pereira, F., Buscaglia, G.C.: The multiscale Robin coupled method for flows in porous media. J. Comput. Phys. **355**, 1–21 (2018)
2. Guiraldello, R.T., Ausas, R.F., Sousa, F.S., Pereira, F., Buscaglia, G.C.: Interface spaces for the multiscale Robin coupled method in reservoir simulation. Math. Comput. Simul., in press
3. Francisco, A., Ginting, V., Pereira, F., Rigelo, J.: Design and implementation of a multiscale mixed method based on a nonoverlapping domain decomposition procedure. Math. Comput. Simul. **99**, 125–138 (2014)
4. Douglas, J., Paes-Leme, P.J., Roberts, J.E., Wang, J.P.: A parallel iterative procedure applicable to the approximate solution of second order partial differential equations by mixed finite element methods. Numer Math. **65**(1), 95–108 (1993)
5. Arbogast, T., Pencheva, G., Wheeler, M.F., method, I.Yotov.: A multiscale mortar mixed finite element. SIAM Multiscale Model Simul. **6**(1), 319–346 (2007)
6. Harder, C., Paredes, D., Valentin, F.: A family of multiscale hybrid-mixed finite element methods for the Darcy equation with rough coefficients. J Comput. Phys. **245**, 107–130 (2013)

7. Larson, M.G., Niklasson, A.J.: A conservative flux for the continuous Galerkin method based on discontinuous enrichment. CALCOLO **41**(2), 65–76 (Jun 2004)
8. Sun, S., Wheeler, M.F.: Projections of velocity data for the compatibility with transport. Comput. Methods Appl. Mech. Eng. **195**(7), 653–673 (2006)
9. Jenny, P., Lee, S., Tchelepi, H.: Multi-scale finite-volume method for elliptic problems in subsurface flow simulation. J. Comput. Phys. **187**(1), 47–67 (2003)
10. Jenny, P., Lee, S., Tchelepi, H.: Adaptive multiscale finite-volume method for multiphase flow and transport in porous media. Multiscale Modeling & Simulation **3**(1), 50–64 (2005)
11. Arbogast, T., Wheeler, M.F., Yotov, I.: Mixed finite elements for elliptic problems with tensor coefficients as cell-centered finite differences. SIAM J. Numer. Anal. **34**(2), 828–852 (1997)
12. Bellin, A., Rubin, Y.: HYDRO_GEN: a spatially distributed random field generator for correlated properties. Stoch. Hydrol. Hydraul. **10**(4), 253–278 (1996)
13. Christie, M., Blunt, M.: Tenth SPE comparative solution project: a comparison of upscaling techniques. SPE-66599-MS Society of Petroleum Engineers (2001)
14. Glowinski, R., Wheeler, M.: Domain decomposition and mixed finite element methods for elliptic problems. First international symposium on domain decomposition methods for partial differential equations, pp. 144–172 (1988)
15. Belgacem, F.: The mortar finite element method with Lagrange multipliers. Numer. Math. **84**(2), 173–197 (1999)
16. Gottlieb, S., Shu, C.: Total variation diminishing Runge-Kutta schemes. Math. Comput. **67**(221), 73–85 (1998)
17. Wolfsteiner, C., Lee, S., Tchelepi, H.: Well modeling in the multiscale finite volume method for subsurface flow simulation. SIAM Multiscale Model. Simul. **5**, 900–917 (2006)